

7 On the Flow Through Bering Strait: A Synthesis of Model Results and Observations

J. Clement Kinney¹; W. Maslowski¹; Y. Aksenov²; B. de Cuevas²; J. Jakacki³; A. Nguyen⁴; R. Osinski¹; M. Steele⁵; R. A. Woodgate⁵; J. Zhang⁵

1. Naval Postgraduate School, Monterey, CA, United States
2. National Oceanography Centre, Southampton, United Kingdom
3. Institute of Oceanology, Polish Academy of Sciences, Sopot, Poland
4. Massachusetts Institute of Technology, Cambridge, MA, United States
5. Applied Physics Laboratory, University of Washington, Seattle, WA, United States

KEYWORDS: Bering Strait, ocean modeling, Pacific water, numerical modeling

Abstract

Bering Strait is the only ocean connection between the Pacific and the Arctic. The flow through this narrow and shallow strait links the Pacific and Arctic oceans and impacts oceanic conditions downstream in the Chukchi Sea and the Western Arctic. We present a model synthesis of exchanges through Bering Strait at monthly to decadal time scales, including results from coupled ice-ocean models and observations. Significant quantities of heat and freshwater are delivered annually into the southern Chukchi Sea via Bering Strait. We quantify seasonal signals, along with interannual variability, over the course of 26 years of multiple model integrations. Volume transport and property fluxes are evaluated among several high-resolution model runs and compared with available moored observations. High-resolution models represent the bathymetry better, and may have a more realistic representation of the flow through the strait, although in terms of fluxes and mean properties, this is not always the case. We conclude that, (i) while some of the models used for Arctic studies achieve the correct order of magnitude for fluxes of volume, heat and freshwater, and have significant correlations with observational results, there is still a need for improvement and (ii) higher spatial resolution is needed to resolve features such as the Alaska Coastal Current (ACC). At the same time, additional measurements with better spatial coverage are needed to minimize uncertainties in observed estimates and to constrain models.

7.1 Introduction

The Pacific Arctic Region spans the sub-Arctic Bering Sea northward through the Chukchi and Beaufort seas and the Arctic Ocean. The Bering Strait, a narrow passageway, connects the wide and shallow shelves of the Bering and Chukchi seas and is the only Pacific connection to the Arctic Ocean. The narrow (~85 km wide) and shallow (~50 m deep) strait provides low-salinity and high-nutrient Pacific Water to the Chukchi Sea and the Arctic Ocean. Many global and regional models face challenges with resolving oceanic exchanges across this narrow and shallow strait, mainly due to the requirement of high spatial resolution and the associated high computational cost to resolve it. In fact, many coarse-resolution models either have a closed Bering Strait or use a prescribed boundary condition. However, Goosse et al. (1997) demonstrated that there is a significant improvement in modeled ocean dynamics in a coarse resolution (3°x3°) model with an opened Bering Strait. They also found that opening Bering Strait

41 produced a more realistically positioned sea ice edge in the Bering Sea, because warm
42 water was allowed to advect further north onto the Bering-Chukchi shelf. Arctic
43 freshwater budgets were also improved, with increased freshwater storage in the
44 Greenland and Norwegian Seas.

45

46 Scientific access across Bering Strait has been restricted due to the political boundary
47 between the United States and Russia. The Russian-US Convention line, dividing the
48 Exclusive Economic Zones (EEZs) of the two countries, lies between two islands near the
49 center of the strait: Ratmanova Island (part of Russia, also called Big Diomedes in the
50 U.S.) and Little Diomedes Island (part of the U.S.). While U.S. research has maintained
51 moorings in the Bering Strait almost continuously since 1990, only for limited portions of
52 that time has U.S. access been granted to the western side of the strait.

53

54 The first goal of this work is to compare state-of-the-art output on the Bering Strait
55 throughflow from several regional and global Arctic-focused models. We will analyze
56 the volume and property fluxes over a long time series (up to 26 years depending on
57 available results from individual models). In addition to interannual changes, we will
58 also examine seasonal cycles in these parameters. The second related goal of this work is
59 to compare model results with the available observational data. These data are from
60 moored instruments placed near-bottom in three point locations in the vicinity of the
61 strait (Fig. 1a). Both observations and models have their own limitations in Bering Strait.
62 Numerical models are limited by relatively coarse resolution in the strait, errors in forcing
63 and omitted processes (e.g., tides), whereas observational results are limited by spatial
64 coverage across the strait, and lack of upper layer measurements.

65 **7.2 Model Descriptions**

66 In this section we describe five global and regional sea ice-ocean coupled models
67 employed to investigate Bering Strait inflow (Tab. 1). The models used in the study have
68 various design features, including resolution, atmospheric forcing, restoring terms,
69 coefficients, and parameterizations. Details of these features for each model are
70 discussed below and shown in Tables 1 and 2. The goal here is to present results on the
71 flow through Bering Strait from a variety of models and assess differences among them
72 and observed data.

73 ***7.2.1 Bering Ecosystem Study ice-ocean Modeling and Assimilation System*** 74 ***(BESTMAS)***

75 BESTMAS (Zhang et al. 2010) is based on the coupled Parallel Ocean and sea Ice
76 Model (POIM) of Zhang and Rothrock (2003). The sea ice model is the multicategory
77 thickness and enthalpy distribution (TED) sea ice model (Zhang and Rothrock 2001;
78 Hibler 1980). It employs a teardrop viscous-plastic rheology (Zhang and Rothrock 2005),
79 a mechanical redistribution function for ice ridging (Thorndike et al. 1975; Hibler 1980),
80 and a LSR (line successive relaxation) dynamics model to solve the ice momentum

81 equation (Zhang and Hibler 1997). The TED ice model also includes a snow thickness
82 distribution model following Flato and Hibler (1995). The ocean model is based on the
83 Parallel Ocean Program (POP) developed at Los Alamos National Laboratory (Smith et
84 al. 1992; Dukowicz and Smith 1994). Given that tidal energy accounts for 60–90% of the
85 total horizontal kinetic energy over the southeastern shelf region of the Bering Sea
86 (Kinder and Schumacher 1981), tidal forcing arising from the eight primary constituents
87 (M2, S2, N2, K2, K1, O1, P1, and Q1) (Gill 1982) is incorporated into the POP ocean
88 model. The tidal forcing consists of a tide generating potential with corrections due to
89 both the earth tide and self-attraction and loading following Marchuk and Kagan (1989).
90 The model domain of BESTMAS covers the northern hemisphere north of 39°N. The
91 BESTMAS finite-difference grid is based on a generalized orthogonal curvilinear
92 coordinate system with a horizontal dimension of 600x300 grid points. The “north pole”
93 of the model grid is placed in Alaska. Thus, BESTMAS has its highest horizontal
94 resolution along the Alaskan coast and in the Bering, Chukchi, and Beaufort seas, with an
95 average of about 7 km for the whole Bering Sea and 10 km for the combined Chukchi
96 and Beaufort seas. There are 26 grid cells across Bering Strait (Fig. 1b), which allows a
97 good connection between the Bering Sea and the Arctic Ocean. The TED sea ice model
98 has 8 categories each for ice thickness, ice enthalpy, and snow depth. The centers of the 8
99 ice thickness categories are 0, 0.38, 1.30, 3.07, 5.97, 10.24, 16.02, and 23.41 m. The POP
100 ocean model has 30 vertical levels of varying thicknesses to resolve surface layers and
101 bottom topography. The first 13 levels are in the upper 100 m and the upper six levels are
102 each 5 m thick. The model bathymetry is obtained by merging the IBCAO (International
103 Bathymetric Chart of the Arctic Ocean) dataset and the ETOPO5 (Earth Topography Five
104 Minute Gridded Elevation Data Set) dataset (see Holland 2000). BESTMAS is forced by
105 daily NCEP/NCAR reanalysis (Kalnay et al. 1996) surface forcing fields. Model forcing
106 also includes river runoff of freshwater in the Bering and Arctic seas. For the Bering Sea,
107 monthly climatological runoffs of the Anadyr, Yukon, and Kuskokwim rivers are used
108 (Zhang et al. 2010). For the Arctic Ocean, monthly climatological runoffs of the Pechora,
109 Ob, Yenisei, Olenek, Yana, Indigirka, Kolyma, Mackenzie, Dvina, Lena, Khatanga,
110 Taimyra, and Piasina rivers are from the Alfred Wegener Institute (Prange and Lohmann
111 2004). Although BESTMAS has a large model domain that includes the Arctic and the
112 North Pacific, realistic lateral open boundary conditions are still necessary to create the
113 right water masses and fluxes. The POP ocean model has been further modified to
114 incorporate open boundary conditions so that BESTMAS is able to be one-way nested to
115 a lower resolution but global POIM (Zhang 2005). Monthly mean open boundary
116 conditions of ocean temperature, salinity, and sea surface height from the global POIM
117 are imposed at the southern boundaries along 39°N. No data were assimilated in
118 BESTMAS.

119 ***7.2.2 Estimating the Circulation and Climate of the Ocean, Phase II (ECCO2)***

120 The ECCO2 regional Arctic Ocean solution uses a configuration of the Massachusetts
121 Institute of Technology general circulation model (MITgcm; Marshall et al. 1997; Losch
122 et al. 2010; Nguyen et al. 2011). The domain boundaries are at ~55° North in both the
123 Atlantic and Pacific sectors. These boundaries coincide with grid cells in a global,

124 cubed-sphere configuration of the MITgcm (Menemenlis et al. 2005).

125
126 The grid covering the Arctic domain is locally orthogonal with horizontal grid spacing
127 of approximately 18 km. There are 50 vertical levels ranging in thickness from 10 m near
128 the surface to approximately 450 m at a maximum model depth of 6150 m. The model
129 employs the rescaled vertical coordinate z^* of Adcroft and Campin (2004) and the
130 partial-cell formulation of Adcroft et al. (1997), which permits accurate representation of
131 the bathymetry. Bathymetry is from the S2004 (W. Smith, 2010, personal
132 communication) blend of the Smith and Sandwell (1997) and the General Bathymetric
133 Charts of the Oceans (GEBCO) one arc-minute bathymetric grid. The non-linear
134 equation of state of Jackett and McDougall (1995) is used. Vertical mixing follows Large
135 et al. (1994). A 7th-order monotonicity-preserving advection scheme of Daru and
136 Tenaud (2004) is employed and there is no explicit horizontal diffusivity. Horizontal
137 viscosity follows Leith (1996) but is modified to sense the divergent flow (Fox-Kemper
138 and Menemenlis 2008).

139
140 The ocean model is coupled to the MITgcm sea ice model described in Losch et al.
141 (2010). Ice mechanics follow a viscous-plastic rheology and the ice momentum
142 equations are solved numerically using the line-successive-over-relaxation (LSOR) solver
143 of Zhang and Hibler (1997). Ice thermodynamics use a zero-heat-capacity formulation
144 and seven thickness categories, equally distributed between zero to twice the mean ice
145 thickness in each grid cell. Ice dynamics use a 2-category thickness with one for open
146 water and one for ice. Salt rejected during ice formation is treated using a sub-grid-scale
147 salt-plume parametrization described in Nguyen et al. (2009). The model includes
148 prognostic variables for snow thickness and for sea ice salinity.

149
150 Initial and lateral boundary conditions come from the globally optimized ECCO2
151 solution (Menemenlis et al. 2008). Surface atmospheric forcing fields are from the
152 Japanese 25-year reanalysis (JRA25; Onogi et al. 2007). Monthly mean river runoff is
153 based on the Arctic Runoff Data Base (ARDB) as prepared by P. Winsor (2007, personal
154 communication). No restoring is used.

155
156 Ocean and sea ice parameters, such as mixing and drag coefficients and albedos, were
157 optimized regionally based on observations (Nguyen et al. 2011). The model results
158 presented here are from a 1992-2008 forward model run using the optimized parameters
159 and do not assimilate any data. The model bathymetry in the vicinity of Bering Strait and
160 the location of the Bering Strait cross-section are shown in Figure 1c. The mean
161 horizontal grid spacing of the model across Bering Strait is 23km.

162 ***7.2.3 Naval Postgraduate School Arctic Modeling Effort (NAME)***

163 The NAME coupled sea-ice–ocean model (Maslowski et al. 2004) has a horizontal grid
164 spacing of $1/12^\circ$ (or ~ 9 km). In the vertical direction, there are 45 vertical depth layers
165 ranging from 5 m near the surface to 300 m at depth, with eight levels in the upper 50 m.
166 The high vertical resolution, especially in the upper water column, allows for more

167 realistic representation of the shallow Arctic and sub-Arctic shelves. In addition, the
168 horizontal grid permits calculation of flow through the narrow straits of the northern
169 Bering Sea (Clement et al. 2005). The model domain is configured in a rotated spherical
170 coordinate system to minimize changes in grid cell area. It contains the sub-Arctic North
171 Pacific (including the Sea of Japan and the Sea of Okhotsk) and North Atlantic Oceans,
172 the Arctic Ocean, the Canadian Arctic Archipelago (CAA) and the Nordic Seas (see Fig.
173 1a of Maslowski et al. 2004 for model domain). The region of interest, the Bering Sea, is
174 therefore far away from the artificially closed lateral boundaries in the North Pacific at
175 30°N, greatly reducing any potential effects of boundary conditions. In an effort to
176 balance the net flow of Pacific Ocean water into the Arctic Ocean, a U-shaped 500 m
177 deep, 162 km (18 grid point) wide channel was created through North America
178 connecting the Atlantic Ocean to the Pacific Ocean. A westward wind forcing of 1.75
179 dyne cm⁻² is prescribed along the channel (see Maslowski et al. 2004 for further details).
180 Flow through the Bering Strait and the channel is not prescribed. There are 15 grid cells
181 across Bering Strait in this model (Fig. 1d). Model bathymetry is derived from two
182 sources: ETOPO5 at 5 km resolution for the region south of 64°N and International
183 Bathymetric Chart of the Arctic Ocean (IBCAO; Jakobsson et al. 2000) at 2.5 km
184 resolution for the region north of 64°N.

185

186 The ocean model was initialized with climatological, 3-dimensional temperature and
187 salinity fields (PHC; Steele et al. 2001) and integrated for 48 years in a spinup mode.
188 During the spinup, daily averaged annual climatological atmospheric forcing derived
189 from 1979 to 1993 reanalysis from the European Centre for Medium-Range Weather
190 Forecasts (ECMWF) was used for 27 years. Next an additional run was performed using
191 repeated 1979 ECMWF annual cycle for six years and then 1979–1981 interannual fields
192 for the last 15 years of the 48-year spinup. This approach is especially important in
193 establishing realistic ocean circulation representative of the time period at the beginning
194 of the actual interannual integration. This final run with realistic daily averaged ECMWF
195 interannual forcing starts in 1979 and continues through 2004. Results from this
196 integration (26 years) are used for the analyses in this chapter. Daily climatological
197 runoff from the Yukon River (and all other major Arctic rivers) is included in the model
198 as a virtual freshwater flux at the river mouth. However, in the Gulf of Alaska the
199 freshwater flux from runoff (Royer 1981) is introduced by restoring the surface ocean
200 level (of 5 m) to climatological (Polar Science Center Hydrographic Climatology; PHC)
201 monthly mean temperature and salinity values over a monthly time scale (as a correction
202 term to the explicitly calculated fluxes between the ocean and underlying atmosphere or
203 sea-ice). Additional details on the model including sea-ice and river runoff have been
204 provided elsewhere (Maslowski et al. 2004).

205 ***7.2.4 Nucleus for European Modelling of the Ocean (NEMO) with ORCA*** 206 ***configuration***

207 The ORCA025-N102 model configuration of the National Oceanography Centre
208 Southampton is an “eddy-permitting” z-level global coupled sea ice-ocean model.
209 ORCA025-N102 was developed within the Nucleus for European Modelling of the

210 Ocean (NEMO) framework for ocean climate research and operational oceanography
211 (<http://www.nemo-ocean.eu/>; Madec 2008) as part of the DRAKKAR configurations
212 (DRAKKAR group 2007) and is largely based on the ORCA025-G70 configuration (e.g.,
213 Lique et al. 2009). ORCA025-N102 includes the ocean circulation model OPA9 (Madec
214 et al. 1998) coupled to the Louvain-la-Neuve Ice Model sea ice model LIM2 (Fichefet
215 and Morales Maqueda 1997). The ocean model is configured on a tri-polar Arakawa C-
216 grid (Arakawa 1966) with the model poles at the geographical South Pole, in Siberia and
217 in the Canadian Arctic Archipelago (CAA). The horizontal resolution is approximately
218 28 km at the equator, increasing to 6-12 km in zonal and ~3 km in meridional directions
219 in the Arctic Ocean. The model resolves large eddies (~30-50 km), while “permitting”
220 most of smaller eddies. ORCA025-N102 has a higher vertical resolution than the
221 ORCA025-G70 configuration, utilizing 64 vertical levels with thicknesses ranging from
222 approximately 6 m near the surface to 204 m at 6000 m. The high vertical resolution in
223 the upper ocean (8 levels in the upper 50 m and 13 levels in the upper 100 m) greatly
224 improves the model representation of the shallow Arctic continental shelves, Bering and
225 Chukchi Seas. There are 8 model cells across Bering Strait (Fig. 1e). The fine model
226 resolution in the both, horizontal and vertical, together with high resolution model
227 bathymetry adapted from ETOPO2 and partial steps in the model bottom topography
228 accurately approximates the steep seabed relief near the Arctic shelves, resulting in the
229 more realistic along-shelf flow (e.g., Barnier et al. 2006; Penduff et al. 2007). The LIM2
230 sea ice model uses the Viscous-Plastic (VP) ice rheology (Hibler 1979) and the 3-layer
231 Semtner (1976) thermodynamics updated with sub-grid scale sea ice thickness
232 distribution (Fichefet and Morales Maqueda 1997) and sea ice thickness-dependent
233 albedo (Payne, 1972). To obtain more distinct sea ice edges, the model employs the
234 positive-definite, second moments conserving advection scheme by Prather (1986). The
235 sea ice model is coupled to the ocean model every five oceanic time steps through a non-
236 linear quadratic drag law (Timmermann et al. 2005).

237

238 For the 1958–2001 simulations used in the present study, the ORCA025 model was
239 driven by the DRAKKAR Forcing Set (DFS 3.1) atmospheric reanalysis (Brodeau et al.
240 2010). The reanalysis combines monthly precipitation, daily downward shortwave and
241 longwave radiation from the CORE forcing data set (Large and Yeager 2004) and 6-
242 hourly 10 m wind, 2 m air humidity and 2 m air temperature from ERA40 reanalysis. The
243 turbulent exchanges between atmosphere and ocean and atmosphere and sea ice are
244 computed during model integration using the bulk formulae from Large and Yeager
245 (2004). Climatological monthly continental runoff (Dai and Trenberth 2002) is included
246 as an additional freshwater source, applied along the coastline. Initial conditions for
247 temperature and salinity are derived from a monthly climatology that merges the Levitus
248 (1998) World Ocean Atlas climatology with the PHC2.1 database (Steele et al. 2001) in
249 high latitudes. To avoid salinity drift, the sea surface salinity is restored toward the
250 monthly mean climatological values on the timescale of 180 days for the open ocean and
251 12 days under sea-ice.

252 **7.2.5 Pan-Arctic Ice-Ocean Modeling and Assimilation System (PIOMAS)**

253 PIOMAS is a variant of BESTMAS (see description above) with a coarser horizontal
254 resolution (~40 km) and smaller model domain (north of 49°N; Zhang et al. 2008).
255 However, it has 12 categories each for ice thickness, enthalpy, and snow depth (Zhang et
256 al. 2008). The centers of the 12 ice thickness categories are 0, 0.26, 0.71, 1.46, 2.61, 4.23,
257 6.39, 9.10, 12.39, 16.24, 20.62, and 25.49 m. The model bathymetry in the vicinity of
258 Bering Strait and the location of the Bering Strait cross-section are shown in Figure 1f.

259 **7.3 Bering Strait Observational Mooring Data**

260 Year-round moorings have been deployed in the strait almost continuously since 1990
261 (see Woodgate et al. 2006, 2010; and <http://psc.apl.washington.edu/BeringStrait.html>),
262 generally at 2-4 locations, as shown in Figure 1a. Site A1 is in the western channel of the
263 strait and thus in the Russian EEZ. Access was only granted to this site in the early 1990s
264 (data available from 90-91; 92-93, 93-94) and since 2004. Site A2 is in the eastern
265 portion of the strait (U.S. waters). A third site, A3, was established in 1990 at a site just
266 north of the strait (and in the US EEZ), hypothesized to provide a useful average of the
267 flow through both of the channels (Woodgate et al. 2005a, b, 2006, 2007). For some
268 years (92-93, 93-94, 94-95) the A3 mooring was deployed ~ 120nm further north, but
269 these data are not considered here. Observations from A2 and A3 are available since
270 autumn 1990, except for a few missing months, and for the deployment year autumn
271 1996-1997 when no moorings were deployed in the strait. A fourth mooring site A4, was
272 established near the U.S. coast in 2001 to measure the Alaskan Coastal Current
273 (Woodgate and Aagaard 2005; see discussion below). A high-resolution array was
274 deployed in the strait starting in 2007; for more details see
275 <http://psc.apl.washington.edu/BeringStrait.html>.

276
277 Since the region is ice-covered in winter, all mooring instrumentation has traditionally
278 been kept near-bottom to avoid damage by ice keels. The moorings provide
279 measurements of temperature, salinity and velocity approximately 10 m above bottom.
280 High correlation (0.95; Woodgate et al. 2005b) in velocity is found between all sites in
281 the strait region (Woodgate et al. 2005b) suggesting that extrapolation of velocity
282 between mooring sites is reasonable. All available ADCP data (some moorings, and
283 ship-based ADCP sections from the eastern channel) and newer mooring data, show
284 strong coherence in the vertical (see e.g., Roach et al. 1995, where the first EOF at a
285 central channel site explains 90% of the variance), with some surface intensification of
286 the flows, especially within the Alaskan Coastal Current. Thus, assuming the near-
287 bottom flow correlates well with the total volume transport also seems reasonable (see
288 Woodgate et al. 2005b for a discussion). In terms of water properties, the near-bottom
289 data do not capture the upper layer, which in the summer/autumn period of the year is
290 likely 10-20 m thick, about 1-2 °C warmer and about 1 psu fresher than the lower layer
291 (Woodgate and Aagaard 2005; Woodgate et al. 2010).

292

293 The flow through the Bering Strait is generally believed to be driven by some far field
294 forcing (often described as the pressure head forcing) modulated by local wind effects
295 (see Woodgate et al. 2005b for discussion and historic references). Woodgate et al.
296 (2005b) suggest this large-scale forcing likely explains the high velocity correlation
297 between sites. On the Alaskan Coast on the edge of the eastern channel there is
298 seasonally a strong surface-intensified current. This is the Alaskan Coastal Current,
299 which is present from midsummer until about the end of the year (Paquette and Bourke
300 1974; Ahlnäs and Garrison 1984; Woodgate and Aagaard 2005), and in summer CTD
301 sections it is present as a ~10 km wide, 40 m deep warm, fresh current (Woodgate and
302 Aagaard 2005). Much less is known about the Siberian Coastal Current (SCC), which is
303 present sometimes on the Russian coast (Weingartner et al. 1999). Observations from the
304 western side of Bering Strait indicate that the SCC can, at times, flow southward here
305 under strong northerly winds. These events tend to occur during autumn and winter and
306 appear to be short-lived (1-10 days; Weingartner et al. 1999). The SCC transport is
307 estimated to be small (~0.1 Sv; Weingartner et al. 1999).

308 **7.4 Results**

309 Model representations of the geographical width across Bering Strait range from 90 –
310 160 km (Fig. 2), in part due to the choice made of the representative section in the model.
311 ORCA and PIOMAS have widths most similar to reality (~85 km), while BESTMAS,
312 NAME, and ECCO2 are wider than reality. The various horizontal resolutions from the
313 five models and the different bathymetry schemes make the results appear disparate upon
314 first glance. In fact the cross-sectional area of the strait varies from 2.4 - 4.5 km² for the
315 models (Tab. 2). However, a closer look suggests agreement that horizontal shear is
316 frequently present in the model results and that the highest speeds tend to be in the
317 eastern channel. It is likely that this is at least in part an artifact due to the way the model
318 sections cross the bathymetry, with the ends of the sections being either north or south of
319 the strait proper. Certainly, observational results (e.g., Woodgate et al. 2005b) show no
320 significant differences in the near-bottom velocity between the two channels away from
321 the ACC. Vertical shear is present in some model results, particularly the NAME,
322 ECCO2, and ORCA models. In NAME, the velocity tends to increase from surface to
323 bottom, in contrast to other models. It appears that the velocity maxima are located
324 deeper in the channels where frictional effects are less, as compared to the surface and
325 nearby the coasts.

326
327 We also present northward velocity, temperature, and salinity sections for the summer
328 period (Jul.-Sep.) from the five models (Figs. 3-5). Strong vertical mixing is expected
329 during the winter period within the northern Bering Sea (Clement et al. 2004; Woodgate
330 and Aagaard 2005). Therefore, we present the mean summer results for comparison.
331 The mean summer velocity sections from the models show slightly higher speeds than the
332 long-term annual mean, especially in the upper water column (Fig. 3). There tends to be
333 less vertical shear in the mean summer sections, as compared to the long-term mean
334 sections (Fig. 2). Temperature sections (Fig. 4) indicate higher values in the upper water
335 column near the Alaskan coast. BESTMAS and NAME have temperature values up to

336 ~10°C here. Similarly, for salinity (Fig. 5) an east-west gradient is present with the lower
337 values found on the eastern side. Particularly, ECCO2, BESTMAS, and NAME show
338 salinities less than 30 psu in this location. Multiple summertime CTD sections of
339 temperature and salinity (<http://psc.apl.washington.edu/BeringStrait.html>) indicate
340 elevated temperature and decreased salinity nearby the U.S. coast due to the presence of
341 the Alaska Coastal Current. The width of this current is on the order of ~10 km and,
342 therefore, it is not properly resolved by the models due to spatial resolution limitations.
343 However, model results do show the proper east-west gradients in temperature and
344 salinity, as expected from observations (see e.g., Coachman et al. 1975).

345
346 To compare with long-term moored observations, we present monthly mean northward
347 near-bottom velocity at sites A2 and A3 for models (color) and data (black) for 1979-
348 2004 in Figure 6. For A2 (eastern channel, Fig. 1a), model velocities range from ~5 cm/s
349 southward to over 80 cm/s northward. Predominantly, the flow is northward with the
350 mean northward velocity ranging from 28.6 (+/- 1.0) to 40.1 (+/- 1.9) cm/s among
351 models, over the time period when observations are available (Tab. 3). The range is 29.5
352 (+/- 0.49) to 43.2 (+/- 0.88) cm/s over the larger 1979-2004 time period (Tab. 4.) Two of
353 the lower resolution models (ORCA and ECCO2) have the highest velocities, while the
354 higher resolution models (BESTMAS and NAME) have lower velocities. The observed
355 mean northward velocity is 26.2 (+/- 2.8) cm/s, which matches the lower range of the
356 modeled mean values. All of the models show a significant (at the 99% level) correlation
357 with the observed velocities at this location. The correlation coefficients range from 0.67
358 to 0.78 for the monthly means at A2 (Tab. 5).

359
360 Figure 3b shows the near-bottom northward velocity at the A3 location. The model
361 spread of velocities is slightly narrower for A3, with the BESTMAS model having the
362 lowest mean velocity (21.8 +/- 0.8 cm/s) and ORCA having the highest mean velocity
363 (30.6 +/- 1.3 cm/s) over the same time period as observations. The observed mean
364 northward velocity is 20.9 +/- 2.3 cm/s. The correlations between the models and the data
365 at A3 are significant (at the 99% level), with correlation coefficients ranging between
366 0.70 and 0.82 (Tab. 5).

367
368 It is important to recognize that a comparison between point measurements and model
369 results is difficult. In the data, velocity is measured at a single point, while in models it is
370 a grid-cell mean, which may range from a few to tens of kilometers in the horizontal and
371 several meters in the vertical. In addition, the discrepancy between the real and model
372 bathymetry introduces a difference in bathymetric gradients, displacing model currents
373 from their “true” geographical positions. Choice of model section location is also very
374 important, for example, there will be obvious discrepancies between an observational
375 section taken across the narrowest point of the strait and a model section crossing shallow
376 regions to the north or south of the strait. Table 6 and Figure 2 illustrate these points.
377 Table 6 shows the depth at the moorings A2 and A3 and model depth at the co-located
378 virtual moorings; the difference between real and model bathymetry is clear. Moreover,
379 in the models, velocity can vary significantly between the adjacent model grid cells (Fig.
380 2), although this is not seen in observations outside the ACC. Thus the results of a
381 model-observations comparison would depend upon the exact geographical position of

382 model virtual moorings. Finally, the stochastic nature of the oceanic turbulence cannot be
383 simulated by the models used in this study. Therefore, it is likely more informative to
384 evaluate model results using integrated fluxes, as discussed below.

385
386 Monthly mean Bering Strait volume transport from the models and observations is
387 shown in Figure 7. The observations are based on the near-bottom velocity at the A3
388 mooring location multiplied by a cross-sectional area of 4.25 km^2 , as per Woodgate et al.
389 (2010). Model means range from $0.67 (+/- 0.03)$ to $1.29 (+/- 0.06)$ Sv (Tab. 3) over the
390 time period when observations are available. The volume transport is highest for the
391 ORCA and ECCO2 models and is lowest for the PIOMAS, BESTMAS and NAME
392 models. The observed estimate of the long-term mean (1991-2004) volume transport
393 through Bering Strait is $0.8 +/- 0.2$ Sv (Woodgate et al. 2005a). This estimate is based on
394 observations at the A3 mooring location, although numbers do not differ significantly if
395 using observations from the other mooring sites.

396
397 Near-bottom monthly mean temperatures at the A2 and A3 mooring locations are
398 shown in Figure 8. (Temperature at A1 is not shown because there are too few data
399 available at this time.) Temperatures tend to be warmer at the southern A2 location, with
400 model means ranging between $-0.96 (+/- 0.09)$ to $1.1 (+/- 0.27)$ °C. The mean observed
401 near-bottom temperature for the same location is $0.27 (+/- 0.3)$. ORCA, ECCO2, and
402 BESTMAS models tend to overestimate the temperature by $0.5 - 0.8$ °C in the mean,
403 while NAME underestimates the temperature by 1.2 °C in the mean. We speculate that
404 the colder temperatures for the NAME model may be related to excessive ice production,
405 especially in polynya regions of the northern Bering Sea. Surprisingly, the PIOMAS
406 temperatures are closest to the observed, despite the fact that it is the lowest resolution
407 model in this study and only has 3 grid points across the strait (Fig. 2). Temperatures at
408 the A3 location are, again, underestimated in the NAME model and overestimated in
409 ORCA, ECCO2, BESTMAS and also in PIOMAS. While the magnitude of the model-
410 data differences may be up to ~ 1 °C in the mean, the models' results are significantly
411 correlated (at the 99% confidence level) with the observations. The correlation
412 coefficients range between $0.73 - 0.88$ at A2 and between $0.70 - 0.86$ at A3 (Tab. 5).
413 There is no trend, either observed or modeled, in the time series shown here. There is,
414 however, a strong seasonal cycle present, which enhances the correlations. The seasonal
415 cycle has been identified by many authors (e.g. Fedorova and Yankinam 1963;
416 Coachman et al. 1975; Roach et al. 1995 and references therein) and was later quantified
417 into a modern climatology by Woodgate et al. (2005a). This seasonal cycle will be
418 discussed below.

419
420 A similar analysis was performed for salinity at the A2 and A3 mooring locations (Fig.
421 9). The mean modeled salinity ranges between $31.7 (+/- 0.06)$ and $33.2 (+/- 0.06)$ psu at
422 A2 and between $32.2 (+/- 0.04)$ and $33.2 (+/- 0.06)$ psu at A3. The mean observed
423 salinities are $32.3 (+/- 0.08)$ at A2 and $32.5 (+/- 0.06)$ at A3. The BESTMAS and
424 PIOMAS models tend to overestimate the salinity, by up to 0.9 psu above the observed
425 mean value, whereas the NAME, ECCO2, and ORCA models have values close to the
426 observed. All of the models' results are significantly correlated (at the 99% confidence
427 level) with the observations of salinity at A2 and A3. The correlation coefficients range

428 between 0.60 and 0.70 at A2 and between 0.39 and 0.59 at A3 (Tab. 5). The correlations
429 are not as high for salinity as they are for temperature, especially at the A3 location.
430 Again, a seasonal cycle of salinity is apparent in the time series (also see Woodgate et al.
431 2005a), however it is not as strong as the seasonal cycle of temperature.

432
433 Annual mean volume transport from models and observations is shown in Figure 10a.
434 Observed volume transport (not including the ACC) ranges from 0.6 – 1 Sv (+/- 0.2 Sv,
435 Woodgate et al. 2006), which is most similar to the estimates from the BESTMAS,
436 NAME, and PIOMAS models. The ACC likely adds around 0.1 Sv to the estimates
437 (Woodgate and Aagaard 2005), thus the true flux is likely slightly higher than shown in
438 Fig. 10a, and closer to the ECCO2 values.

439
440 Heat fluxes through Bering Strait and through the Chukchi shelf appear to influence
441 the distribution and thickness of sea ice (Coachman et al. 1975; Shimada et al. 2006;
442 Woodgate et al. 2010). Previously published observations of heat flux (e.g., Woodgate et
443 al. 2010) use a reference temperature of -1.9°C . Therefore, for the model calculations,
444 we used the same value for a reference temperature. However, we note that the PIOMAS
445 and BESTMAS models use -1.8°C as the freezing temperature for an ease in conserving
446 heat in the models. Oceanic heat flux through Bering Strait in the models was calculated
447 as the vertical and horizontal integral of: the heat (heat capacity multiplied by the
448 difference between the temperature and the reference temperature) multiplied by velocity
449 normal to the cross-section on a monthly mean time scale.

450
451 The annual mean oceanic heat flux time series for the models and observations (as per
452 Woodgate et al. 2010) are shown in Figure 10b. In the models, peaks in the heat flux
453 occurred during several years (e.g., 1979, 1986, 1993, and 1997) and consistently showed
454 up in results from all five models. However, data coverage is not sufficient to confirm
455 these peaks in the real world. A peak in 2004 is noted in observations (see Woodgate et
456 al. 2010) and is apparent in all of the models, except ORCA, which does not have results
457 for that time period. ECCO2 is also able to simulate a recent increase in heat flux in 2007
458 (not shown), similar to the observations (Woodgate et al. 2010).

459
460 The long-term model mean heat flux ranged between $1.5 - 5.1 \times 10^{20}$ J/yr. This is,
461 admittedly, a wide range of values. ORCA and ECCO2 have much higher values than
462 BESTMAS and NAME. Observations of the annual heat flux based on near-bottom
463 measurements, a correction for the ACC, and SST from satellite data were published in
464 Woodgate et al. (2010). The observed range of heat flux estimates is $\sim 2.8 - 4.5 \times 10^{20}$ J/yr
465 with estimated uncertainty of 0.8×10^{20} J/yr, based on years 1991, 1998, 2000-2006.
466 However, the 2007 heat flux was estimated at $5-6 \times 10^{20}$ J/yr.

467
468 Freshwater flux from the Bering Sea into the Chukchi Sea is an important factor
469 affecting stratification and the maintenance of the Arctic Ocean halocline (e.g., Aagaard
470 et al. 1985a). As discussed in Aagaard et al. (2006), the salinity field in Bering Strait is
471 influenced by a number of processes primarily within the Bering Sea, including inflow
472 from the Gulf of Alaska, on-shelf transport from the deep basin, precipitation minus
473 evaporation, river runoff, and formation/degradation of sea ice. The combined net effect

474 of these processes determine, in large part, the downstream salinity (and to a lesser extent
475 freshwater fluxes) found in the strait. For the calculation of freshwater fluxes, a reference
476 salinity of 34.8 psu was used because this value is considered to be the mean salinity of
477 the Arctic Ocean and has been used in most other Arctic studies (based on original work
478 by Aagaard and Carmack 1989). Integrated annual mean oceanic freshwater fluxes were
479 calculated on a monthly mean timescale (see Eq. 1 in Melling 2000) from each of the
480 models and are shown in Figure 10c. An observationally-based lower bound of annual
481 mean freshwater fluxes is also shown, however these values do not include the ACC or
482 stratification and thus likely underestimate the freshwater flux by about 800-1,000 km³/yr
483 (Woodgate et al. 2006). With this correction, the observed freshwater annual means are
484 similar to results from the ECCO2 and ORCA models, with the other models appearing
485 to underestimate the total freshwater flux. No long-term trend is apparent in either the
486 heat or freshwater flux for this time period, however a gradual increase in freshwater
487 during the early 2000s has occurred in the model results, ending with a peak in freshwater
488 flux in 2004, similar to observations (also see Woodgate et al. 2006, 2010).

489

490 It is important to note that both the models and the data have limitations with respect to
491 calculations of heat and freshwater fluxes. The models used here are too coarse to
492 represent the narrow (~10 km) Alaska Coastal Current (ACC), which is estimated to
493 carry 25% of the freshwater flux and 20% of the heat flux (Woodgate et al. 2006) through
494 the strait. The historic near-bottom data used here does not measure the ACC, which is a
495 surface/coastal feature. Thus, on-going research is using extra moorings, hydrographic
496 data and upper water column sensors to estimate stratification (see e.g.,
497 <http://psc.apl.washington.edu/BeringStrait.html>).

498

499 Arctic shelf seas have a strong seasonal cycle of temperature and salinity; some areas
500 may also exhibit strong seasonal changes in the oceanic circulation. The Bering Strait
501 region is no different in this respect. Observations have shown stronger northward flows
502 in summer (e.g., Coachman and Aagaard 1988; Roach et al. 1995; Woodgate et al. 2005a,
503 b). According to the model results, volume transport peaks in summer (May - July) and
504 is lowest in winter (December – March; Fig. 11). This agrees reasonably with
505 observational results (peaking in May/Jun, minimum in Dec-Feb; although variability is
506 high; Woodgate et al. 2005a). In general, the data have a larger seasonal cycle, with a
507 range of 0.4 to 1.3 Sv (errors order 25%; Woodgate et al. 2005a, b). PIOMAS,
508 BESTMAS, ECCO2, and NAME models have similar seasonal cycles to the data,
509 however they are not as strong.

510

511 As shown by Woodgate et al. (2010), the heat flux seasonal cycle is also very strong.
512 Observational results (see Fig. 3 of Woodgate et al. 2010) suggest strong interannual
513 variability in the timing of the summer peak, although the computation presented there
514 does not include the seasonality of the ACC. In the models (Fig. 11), heat flux peaks in
515 summer and is near-zero in winter. However, the models do not agree on the magnitude
516 of the summertime peak, which ranges between 15 (+/- 6.4) to over 40 (+/- 14) TW. The
517 heat flux is near zero for December – April (when water temperatures are around
518 freezing). The models with the highest resolutions (BESTMAS and NAME) show lower

519 peaks in the summertime heat flux [15 (+/- 6.4) and 22.5 (+/- 7.9) TW], while the lower
520 resolution models have higher heat fluxes.

521

522 Seasonal cycles of freshwater flux through Bering Strait are similar for PIOMAS,
523 BESTMAS, and NAME, with peaks in the summer (June – August) and lowest in winter
524 (December – April). Again, interannual variability makes these peaks less certain. The
525 freshwater flux maxima for these models are between 65 (+/- 14.3) - 80 (+/- 13.4) mSv in
526 July. Seasonal cycles for ECCO2 and ORCA have somewhat similar shapes, however
527 they transport more freshwater (up to 115 (+/- 11.7) mSv in summer and more than 60
528 (+/- 40) mSv in winter for ORCA) to the north.

529 **7.5 Summary and Discussion**

530 Model volume transports ranged from 0.67 (+/- 0.03) - 1.29 (+/- 0.06) Sv in the mean,
531 compared to observational estimates of 0.8 +/-0.2 Sv; the observations may still
532 underestimate the ACC contribution. Thus, most of the models are in agreement with the
533 observational estimate to within errors. ORCA and ECCO2 showed the highest volume
534 transports, while NAME and BESTMAS showed the lowest transports. Oddly, higher
535 resolution models seem to give lower transport estimates; we do not fully understand why
536 this is. Note that of the models, ORCA and ECCO2 also have the largest cross sectional
537 area of the strait. The cross-sections in each model were chosen to approximate the
538 locations of moored observations as closely as possible (Fig. 1), however different cross-
539 sectional areas would arise from choosing a slightly different position of the section. The
540 models are using both lateral and vertical friction parameterization to represent the flow
541 next to the boundary (bottom/surface or lateral; see Tab. 2). Some uncertainty of model
542 estimates of the volume transport throughout the strait might be related to the estimation
543 of the frictional layers, subject to the parameterization used. Penduff et al. (2007) have
544 demonstrated that enstrophy-conserving momentum advection schemes produce a
545 spurious numerical sidewall friction, leading to a weaker topographic alignment of the
546 mean flow and weaker barotropic transports. They reported a ~10% reduction in Bering
547 Strait transports in simulations with the enstrophy conserving advection, compared to the
548 runs with the energy-enstrophy conserving scheme, characterized by low numerical
549 friction. The effect of spurious friction on transports is similar to the one of explicit
550 lateral friction. Both spurious sidewall and explicit non-slip lateral friction could explain
551 lower transports in BESTMAS and NAME models compared to ECCO2 and ORCA, as
552 the last two models feature free-slip lateral boundary conditions. Besides, ORCA utilizes
553 energy-enstrophy conserving advection, which may result in higher transport than in
554 ECCO2 (Tables 3 and 4). However, this cannot explain a higher transport in the PIOMAS
555 model compared to BESTMAS, since these two models share the same configuration,
556 except for the resolution and different number of sea ice categories (12 and 8
557 respectively). Thus, another possibility is that different transports reflect different large-
558 scale forcings of the flow.

559

560 Panteleev et al. (2010) applied an inverse model (with 10 grid points across the strait)
561 to reconstruct the flow using available data for 1990-1991 and recently calculated the

562 transport through Bering Strait as 0.57 Sv (no stated uncertainty). The data used to
563 reconstruct the circulation were from 12 moorings that were deployed in the Bering Strait
564 and Chukchi Sea from September 1990 to October 1991 (Woodgate et al. 2005b). This
565 estimate from Panteleev et al. (2010) tends to agree with the estimates from the
566 BESTMAS and NAME models. In fact, the mean volume transports during the same
567 time period (Sept. 1990 – Oct. 1991) were 0.62 (+/- 0.03) and 0.59 (+/- 0.03) Sv for the
568 BESTMAS and NAME models, respectively.

569
570 The model sections presented here show significant vertical and horizontal velocity
571 shear across the strait. This is in contrast to observational results, which show strong
572 coherence of flow and agreement of speeds in the centers of the 2 channels of the strait,
573 and stronger flow in the ACC. The only currently published sections of observed
574 velocity in the strait are those of Coachman et al. (1975), but as the authors themselves
575 point out, these sections are subject to time aliasing being taken over a period of days.
576 Mooring data shows that the cross-strait velocity variability found outside the ACC on
577 those sections can be explained by temporal variability of the flow.

578
579 It seems likely that the variability found in the models is due to edge effects and/or the
580 poor resolution of the real world bathymetry and the exact choice of model section. The
581 lesson to be learned here is that a coarse resolution model cannot be used to study the
582 details of features at the same resolution as the model (e.g. the ACC width of ~10 km). It
583 must also be remembered however, that the observational transports presented here are
584 based on an assumption of homogeneity of flow at all locations in the strait. This is being
585 tested currently by an increased mooring effort in the strait region. Preliminary results
586 suggest this assumption to be reasonably sound outside the ACC region, but more
587 analysis remains to be done.

588
589 It seems inevitable that the seasonally-intensified Alaska Coastal Current (ACC)
590 volume transport is not accounted for in models due to spatial resolution limitations. In
591 order to resolve the ACC, models with higher spatial resolution will need to be employed,
592 while maintaining large model domains to obtain proper water mass transformations and
593 circulations. At the same time, the estimates presented here from observations also lack
594 continuous measurements in the surface layers and near the coast. Although estimates of
595 the contributions from the ACC and stratification have been made by Woodgate et al.
596 (2006, 2010), interannual quantification of the seasonal contribution by the ACC to the
597 overall Bering Strait transport is yet to be computed from either observations or models.
598 The freshwater flux, which has a significant influence on the density structure of the
599 Arctic Ocean (e.g., Aagaard et al. 1985b), would also be better measured if more salinity
600 information could be obtained in the upper layers and especially nearby the coast (see
601 e.g., Woodgate and Aagaard 2005 for discussion). Similarly, for heat flux, it is crucial to
602 get information on the upper layers where maybe 1/3rd of the heat is advected [see
603 Woodgate et al. (2010) who used satellite-derived sea surface temperatures to estimate
604 the contribution from the upper layers]. An international effort is currently underway
605 with 8 moorings placed in the Bering Strait region. New information from these
606 moorings will be important for better understanding details of the flow through the strait.

607

608 While it is encouraging that, in many of the larger-scale models, fluxes of volume, heat
609 and salt are of the right order of magnitude and in interannual terms show correlated
610 variations with observations, there are still significant discrepancies. These have to be
611 considered when using model results to look at the role of Pacific waters in the Arctic.
612 We also see a need for model results with higher spatial resolution in the strait region.
613 The ACC is only order 10 km in width and thus not resolved by global or regional Arctic
614 models with resolutions of 4-40 km (Tab. 1). The implementation of higher-resolution (2
615 km or less) regional models should improve estimates of the volume, heat and freshwater
616 fluxes in the strait, if the issues of large-scale boundary conditions for such a model can
617 be solved. The challenge is to be able to capture small-scale features, such as the Alaska
618 Coastal Current and mesoscale eddies in the strait itself and its immediate vicinity. The
619 modeling community is working toward that goal to properly represent such features.

620
621 **Acknowledgments** We thank the Department of Energy Earth System Modeling program (J. C. K and W.
622 M.), National Science Foundation Office of Polar Programs (J. C. K, W. M., M. S., and J. Z.), and the
623 Office of Naval Research (J. C. K and W. M.) for support of this research. We also thank the Arctic Ocean
624 Model Intercomparison Project (J. C. K. and W. M.) for travel support and for conference opportunities to
625 present and discuss this research. Support for this work was provided (in part) by NSF grants ARC-
626 0632154, ARC-0855748, and the NOAA-RUSALCA program (R. W.). The mooring data used in this
627 study was collected under funding from ONR, NSF, MMS, AOOS and NOAA-RUSALCA (R. W.). At the
628 National Oceanography Centre Southampton (Y.A. and B. d C.) the study was supported by the UK
629 Natural Environment Research Council as a contribution to the Marine Centres' Strategic Research
630 Programme Oceans 2025. The NOCS-ORCA simulations were performed as part of the DRAKKAR
631 collaboration (Barnier et al., 2006). NOCS also acknowledges the use of UK National High Performance
632 Computing Resource. We also thank the editors of this book and two anonymous reviewers for insightful
633 comments, which improved an earlier version of this manuscript.

634 7.6 References

- 635 Aagaard K, Roach AT, Schumacher JD (1985a) On the wind-driven variability of the
636 flow through Bering Strait. *J Geophys Res* 90:7213–7221
637
- 638 Aagaard K, Swift JH, Carmack EC (1985b) Thermohaline circulation in the arctic
639 Mediterranean seas. *J Geophys Res* 90:4833–4846
640
- 641 Aagaard K, Carmack EC (1989) The role of sea-ice and other fresh water in the Arctic
642 circulation. *J Geophys Res* 94:14485–14498
643
- 644 Aagaard K, TJ Weingartner, SL Danielson, RA Woodgate, GC Johnson, TE Whitledge
645 (2006) Some controls on flow and salinity in Bering Strait. *Geophys Res Lett*
646 33:L19602, doi:10.1029/2006GL026612
647
- 648 Adcroft A, Campin JM (2004) Rescaled height coordinates for accurate representation of
649 free-surface flows in ocean circulation models. *Ocean Modelling* 7(3-4):269–284
650
- 651 Adcroft A, Hill C, Marshall J (1997) The representation of topography by shaved cells in
652 a height coordinate model. *Mon Weather Rev* 125(9):2293–2315

653
654 Ahlnäs K, Garrison GR (1984) Satellite and oceanographic observations of the warm
655 coastal current in the Chukchi Sea. *Arctic* 37:244–254
656
657 Arakawa A (1966) Computational design of long-term numerical integration of the
658 equations of fluid motion. *J Comput Phys* 1:119–143
659
660 Barnier B, Madec G, Penduff T, Molines JM, Treguier AM, Le Sommer J, Beckmann A,
661 Biastoch A, Böning C, Dengg J, Derval C, Durand E, Gulev S, Remy E, Talandier C,
662 Theetten S, Maltrud M, McClean J, de Cuevas BA (2006) Impact of partial steps and
663 momentum advection schemes in a global ocean circulation model at eddy permitting
664 resolution. *Ocean Dyn* 56:543–567. doi: 10.1007/s10236-006-0082-1
665
666 Brodeau L, Barnier B, Treguier AM, Penduff T, Gulev S (2010) An ERA40-based
667 atmospheric forcing for global ocean circulation models. *Ocean Modelling* 31(3-4):88–
668 104. doi: 10.1016/j.ocemod.2009.10.005
669
670 Clement JL, Cooper LW, Grebmeier JM (2004) Late winter water column and sea ice
671 conditions in the northern Bering Sea. *Journal of Geophysical Research* 109(C3):
672 C03022, doi: 10.1029/2003JC002047.
673
674 Clement JL, Maslowski W, Cooper L, Grebmeier J, Walczowski W (2005) Ocean
675 circulation and exchanges through the northern Bering Sea - 1979-2001 model results.
676 *Deep Sea Res II* 52:3509–3540. doi: 10.1016/j.dsr2.2005.09.010
677
678 Coachman LK, Aagaard K, Tripp RB (1975) *Bering Strait: The regional physical*
679 *oceanography*. University of Washington Press, Seattle
680
681 Coachman LK, Aagaard K (1988) *Transports through Bering Strait: Annual and*
682 *Interannual Variability*. *J Geophys Res* 93:15,535-15,539.
683
684 Dai A, Trenberth KE (2002) Estimates of freshwater discharge from continents:
685 latitudinal and seasonal variations. *J Hydroeteorol* 3: 660–687
686
687 Daru V, Tenaud C (2004) High order one-step monotonicity-preserving schemes for
688 unsteady compressible flow calculations. *J Comput Phys* 193(2):563–594. doi:
689 <http://dx.doi.org/10.1016/j.jcp.2003.08.023>
690
691 DRAKKAR Group (2007) Eddy-permitting ocean circulation hindcasts of past decades.
692 *CLIVAR Exchanges* No 42:12(3) 8–10
693
694 Dukowicz JK, Smith RD (1994) Implicit free-surface method for the Bryan-Cox-Semtner
695 ocean model. *J Geophys Res* 99:7791–8014
696
697 Fedorova A.P, A.S, Yankina (1964) The passage of Pacific Ocean water through the
698 Bering Strait into the Chukchi Sea. *Deep-Sea Res* 11:427-434

699
700 Fichefet T, Morales Maqueda MA (1997) Sensitivity of a global sea ice model to the
701 treatment of ice thermodynamics and dynamics. *J Geophys Res* 102(C6):12609–12646
702
703 Flato GM, Hibler WD III (1995) Ridging and strength in modeling the thickness
704 distribution of Arctic sea ice. *J Geophys Res* 100:18,611–18,626
705
706 Fox-Kemper B, Menemenlis D (2008) Can large eddy simulation techniques improve
707 mesoscale rich ocean models? In: Hecht M, Hasumi H (eds) *Ocean Modeling in an*
708 *Eddy Regime*, AGU, Washington, D.C
709
710 Gill A (1982) *Atmosphere-Ocean Dynamics*. Academic Press Inc, Burlington, MA
711
712 Goosse H, Campin JM, Fichefet T, Deleersnijder E (1997) Sensitivity of a global ice–
713 ocean model to the Bering Strait throughflow. *Climate Dynamics* 13(5): 349–358
714
715 Hibler WD III (1979) A dynamic thermodynamic sea ice model. *J Phys Oceanogr* 9(4):
716 815–846
717
718 Hibler WD III (1980) Modeling a variable thickness sea ice cover. *Mon Weather Rev*
719 108:1943–1973
720
721 Holland DM (2000) Merged IBCAO/ETOPO5 Global Topographic Data Product.
722 National Geophysical Data Center (NGDC), Boulder CO.
723 <http://www.ngdc.noaa.gov/mgg/bathymetry/arctic/ibcaorelatedsites.html>. Cited 25
724 Dec 2000
725
726 Jackett DR, McDougall TJ (1995) Minimal adjustment of hydrographic profiles to
727 achieve static stability. *J Atmos Oceanic Technol* 12(2):381–389
728
729 Jakobsson M, Cherkis N, Woodward J, Macnab R, Coakley B (2000) New grid of Arctic
730 bathymetry aids scientists and mapmakers. *Eos Trans AGU* 81(9):89
731
732 Kalnay E et al (1996) The NCEP/NCAR 40-year reanalysis project. *Bull Amer Meteorol*
733 *Soc* 77:437–471
734
735 Kinder TH, Schumacher JD (1981) Circulation over the continental shelf of the
736 Southeastern Bering Sea. In: Hood DW, Calder JA (eds) *The eastern Bering Sea shelf:*
737 *Oceanography and resources*, University of Washington Press, Seattle
738
739 Large WG, Pond S (1981) Open ocean momentum flux measurements in moderate to
740 strong winds. *J Phys Ocean* 11(3):324–336
741
742 Large WG, Pond S (1982) Sensible and latent-heat flux measurements over the ocean. *J*
743 *Phys Ocean* 12(5):464–482
744

745 Large W G, McWilliams JC, Doney S (1994) Oceanic vertical mixing: A review and a
746 model with a nonlocal boundary layer parameterization. *Rev Geophysics* 32(4):363–
747 403
748

749 Large WG, Yeager SG (2004) Diurnal to decadal global forcing for ocean and sea-ice
750 models: The data sets and flux climatologies. Technical Report TN-460+STR, NCAR,
751 105pp
752

753 Leith CE (1996) Stochastic models of chaotic systems. *Physica D* 98:481–491
754

755 Levitus S, Boyer TP, Conkright ME, O’Brian T, Antonov J, Stephens C, Stathopoulos L,
756 Johnson D, Gelfeld R (1998) World ocean database 1998. NOAA Atlas NESDID 18,
757 US Government Printing Office, Washington, DC
758

759 Lique C, Treguier AM, Scheinert M, Penduff T (2009) A model-based study of ice and
760 freshwater transport variability along both sides of Greenland. *Clim Dyn* 33:685–705,
761 doi:10.1007/s00382-008-0510-7
762

763 Losch M, Menemenlis D, Heimbach P, Campin JM, Hill C (2010) On the formulation of
764 sea-ice models. part 1: effects of different solver implementations and
765 parameterizations. *Ocean Modelling* 33:129–144
766

767 Madec G, Delecluse P, Imbard M, Levy C (1998) OPA 8.1 ocean general circulation
768 model reference manual. IPSL Tech. Rep. Tech Rep. 11, Institut Pierre-Simon
769 Laplace, 91pp
770

771 Madec G (2008) NEMO reference manual, ocean dynamic component: NEMO-OPA.
772 Rep. 27, Note du pôle de modélisation, Institut Pierre Simmon Laplace (IPSL), France.
773 ISSN No. 1288-1619
774

775 Marchuk GI, Kagan BA (1989) Dynamics of Ocean Tides. Kluwer Academic Publishers,
776 Heidelberg
777

778 Marshall J, Adcroft A, Hill C, Perelman L, Heisey C (1997) A finite-volume,
779 incompressible Navier-Stokes model for studies of the ocean on parallel computers. *J*
780 *Geophys Res* 102(C3): 5753–5766
781

782 Maslowski W, Marble D, Walczowski W, Schauer U, Clement JL, Semtner AJ (2004) On
783 climatological mass, heat, and salt transports through the Barents Sea and Fram Strait
784 from a pan-Arctic coupled ice-ocean model simulation. *J Geophys Res* 109 C03032,
785 doi:10.1029/2001JC001039
786

787 Melling H (2000) Exchanges of fresh-water through the shallow straits of the North
788 American Arctic. In: Lewis EL et al. (eds) *The Fresh-water Budget of the Arctic*
789 *Ocean. Proceedings of a NATO Advanced Research Workshop, Tallinn Estonia, 27*
790 *April – 1 May 1998, Kluwer Academic Publishers Dordrecht Netherlands*

791
792 Menemenlis D, Hill C, Adcroft A, Campin J, Cheng B, Ciotti B, Fukumori I, Heimbach
793 P, Henze C, Koehl A, Lee T, Stammer D, Taft J, Zhang J (2005) NASA supercomputer
794 improves prospects for ocean climate research. *Eos Trans AGU* 86 (9):89, 95–96
795
796 Menemenlis D, Campin J, Heimbach P, Hill C, Lee T, Nguyen A, Schodlok M, Zhang H
797 (2008) ECCO2: High resolution global ocean and sea ice data synthesis. *Mercator*
798 *Ocean Quarterly Newsletter* 31:13–21
799
800 Nguyen AT, Menemenlis D, Kwok R (2009) Improved modeling of the Arctic halocline
801 with a subgrid-scale brine rejection parameterization. *J Geophys Res* 114:C11014,
802 doi:10.1029/2008JC005121
803
804 Nguyen AT, Menemenlis D, Kwok R (2011) Arctic ice-ocean simulation with optimized
805 model parameters: approach and assessment. *J Geophys Res* 116:C04025,
806 doi:10.1029/2010JC006573
807
808 Onogi K, Tsutsui J, Koide H, Sakamoto M, Kobayashi S, Hatsushika H, Matsumoto T,
809 Yamazaki N, Kamahori H, Takahashi K, Kadokura S, Wada K, Kato K, Oyama R, Ose
810 NMT, Taira R (2007) The jra-25 reanalysis. *J Meteor Soc Japan* 85(3):369–432
811
812 Panteleev GG, Nechaev D, Proshutinsky AY, Woodgate R, Zhang J (2010)
813 Reconstruction and analysis of the Chukchi Sea circulation in 1990-1991. *J Geophys*
814 *Res* 115:C08023, doi:10.1029/2009JC005453
815
816 Paquette RG, Bourke RH (1974) Observations on the Coastal Current of Arctic Alaska. *J*
817 *Mar Res* 32:195-207
818
819 Payne RE (1972) Albedo at the sea surface. *J Atmos Sci* 29:959–970
820
821 Penduff T, Le Sommer J, Barnier B, Treguier AM, Molines JM, Madec G (2007)
822 Influence of numerical schemes on current-topography interactions in 1/4° global
823 ocean simulations. *Ocean Sci* 3:509-524
824
825 Prange M, Lohmann G (2004) Variable freshwater input to the Arctic Ocean during the
826 Holocene: implications for large-scale ocean-sea ice dynamics as simulated by a
827 circulation model. In: Fischer H et al. (eds) *The KIHZ project: towards a synthesis of*
828 *Holocene proxy data and climate models*, Springer, New York
829
830 Prather MC (1986) Numerical advection by conservation of second-order moments. *J*
831 *Geophys Res* 91:6671–6681
832
833 Roach AT, Aagaard K, Pease CH, Salo SA, Weingartner T, Pavlov V, Kulakov M (1995)
834 Direct measurements of transport and water properties through the Bering Strait. *J*
835 *Geophys Res* 100:18443-18457
836

837 Royer TC (1981) Baroclinic transport in the Gulf of Alaska, part II. A freshwater driven
838 coast current. *Journal of Marine Research* 39:251-266
839
840 Semtner AJ (1976) A model for the thermodynamic growth of sea ice in numerical
841 investigation of climate. *J Phys Oceanogr* 6:376-389
842
843 Shimada K, Kamoshida T, Itoh M, Nishino S, Carmack E, McLaughlin F, Zimmermann
844 S, Proshutinsky A (2006) Pacific Ocean inflow: influence on catastrophic reduction of
845 sea ice cover in the Arctic Ocean. *Geophys Res Lett* 33:L08605,
846 doi:10.1029/2005GL025624
847
848 Smith RD, Dukowicz JK, Malone RC (1992) Parallel ocean general circulation modeling,
849 *Physica D* 60:38–61
850
851 Smith WHF, Sandwell DT (1997) Global sea floor topography from satellite altimetry
852 and ship depth soundings. *Science* 277(5334):1956–1962
853
854 Steele M, Morley R, Ermold W (2001) PHC: a global ocean hydrography with a high
855 quality Arctic Ocean. *J Clim* 14(9):2079–2087
856
857 Thorndike AS, Rothrock DA, Maykut GA, Colony R (1975) The thickness distribution of
858 sea ice. *J Geophys Res* 80:4501–4513
859
860 Timmermann R, Goose H, Madec G, Fichefet T, Ethe C, Duliere V (2005) On the
861 representation of high latitude processes in the ORCA-LIM global coupled sea ice-
862 ocean model. *Ocean Modelling* 8:175–201
863
864 Weingartner TJ, Danielson S, Sasaki Y, Pavlov V, Kulakov M (1999) The Siberian
865 Coastal Current: a wind- and buoyancy-forced Arctic coastal current. *J Geophys Res*
866 104:29697-29713, doi:10.1029/1999JC900161
867
868 Woodgate RA, Aagaard K (2005) Revising the Bering Strait freshwater flux into the
869 Arctic Ocean. *Geophys Res Lett* 32:L02602, doi:10.1029/2004GL021747
870
871 Woodgate RA, Aagaard K, Weingartner TJ (2005a) Monthly temperature, salinity, and
872 transport variability of the Bering Strait throughflow. *Geophys Res Lett* 32:L04601,
873 doi:10.1029/2004GL021880
874
875 Woodgate RA, Aagaard K, Weingartner TJ (2005b) A year in the physical oceanography
876 of the Chukchi Sea: Moored measurements from autumn 1990-1991. *Deep Sea Res II*
877 52:3116-3149, doi:10.1016/j.dsr2.2005.10.016
878
879 Woodgate RA, Aagaard K, Weingartner TJ (2006) Interannual Changes in the Bering
880 Strait Fluxes of Volume, Heat and Freshwater between 1991 and 2004. *Geophys Res*
881 *Lett* 33:L15609, doi:10.1029/2006GL026931
882

883 Woodgate RA, Aagaard K, Weingartner TJ (2007) First steps in calibrating the Bering
884 Strait throughflow: Preliminary study of how measurements at a proposed climate site
885 (A3) compare to measurements within the two channels of the strait (A1 and A2). 20
886 pp, University of Washington
887

888 Woodgate RA, Weingartner TJ, Lindsay RW (2010) The 2007 Bering Strait oceanic heat
889 flux and anomalous Arctic sea-ice retreat. *Geophys Res Lett* 37:L01602,
890 doi:10.1029/2009GL041621
891

892 Zhang J, Hibler WD (1997) On an efficient numerical method for modeling sea ice
893 dynamics. *J Geophys Res* 102:8691–8702
894

895 Zhang J, Rothrock DA (2001) A thickness and enthalpy distribution sea-ice model. *J*
896 *Phys Oceanogr* 31:2986–3001
897

898 Zhang J, Rothrock DA (2003) Modeling global sea ice with a thickness and enthalpy
899 distribution model in generalized curvilinear coordinates. *Mon Weather Rev* 131:681–
900 697
901

902 Zhang J (2005) Warming of the arctic ice-ocean system is faster than the global average
903 since the 1960s. *Geophys Res Lett*. doi:10.1029/2005GL024216
904

905 Zhang J, Rothrock DA (2005) The effect of sea-ice rheology in numerical investigations
906 of climate. *J Geophys Res*. doi:10.1029/2004JC002599
907

908 Zhang J, Steele M, Lindsay RW, Schweiger A, Morison J (2008) Ensemble one-year
909 predictions of arctic sea ice for the spring and summer of 2008. *Geophys Res Lett*.
910 doi:10.1029/2008GL033244
911

912 Zhang J, Woodgate R, Moritz R (2010) Sea ice response to atmospheric and oceanic
913 forcing in the Bering Sea. *J Phys Oceanogr.* 40, 1729–1747 doi:
914 10.1175/2010JPO4323.1.
915
916
917
918
919
920
921
922
923
924
925
926
927
928

929 **7.7 Tables**

930

931 **Table 1** Basic information on the five models used in this study.

932

Model	Global/Regional	Atmospheric Forcing	Resolution in Bering Strait	Data Assimilation?
BESTMAS	regional	NCEP/NCAR reanalysis	~4 km	no
ECCO2	regional	Japanese 25-year reanalysis	~23 km	no
NAME	regional	ECMWF reanalysis	~9 km	no
ORCA	global	DRAKKAR Forcing Set (DFS 3.1) reanalysis	~13 km	no
PIOMAS	regional	NCEP/NCAR reanalysis	~40 km	no

933

934

935

936

937

938

939

940

941

942

943

944

945

946

947

948

949

950

951

952

953

954

955

956

957

958

959 **Table 2** Cross-sectional area across Bering Strait for the models and observations and
 960 friction coefficients for the models.

961

962

Model/Observed	Area (km ²)	Bottom Friction Coefficient	Lateral Boundary Condition	Lateral Friction Coefficient	Surface Friction Coefficient	
					Ice-Ocean	Air-Ocean
BESTMAS	3.24	quadratic bottom drag: 1.225×10^{-3}	no-slip	variable momentum harmonic horizontal mixing depending on variable grid size	5.5×10^{-3}	1.0×10^{-3}
ECCO2	4.50	quadratic bottom drag: 2.1×10^{-3}	free-slip	modified Leith [Fox-Kemper and Menemenlis, 2008]	5.4×10^{-3}	Large and Pond (1981, 1982)
NAME	2.37	quadratic bottom drag: 1.225×10^{-3}	no-slip	momentum biharmonic horizontal mixing: -1.25×10^{18}	5.5×10^{-3}	0.6×10^{-3}
Observed	2.60	N/A	N/A	N/A	N/A	N/A
ORCA	4.17	quadratic bottom drag: 1.0×10^{-3}	free-slip	bi-harmonic ($-1.5e+11$ m ⁴ /s)	quadratic, 5.0×10^{-3}	CORE bulk formulae, Large and Yeager (2004)
PIOMAS	2.38	quadratic bottom drag: 1.225×10^{-3}	no-slip	variable momentum harmonic horizontal mixing depending on variable grid size	5.5×10^{-3}	1.0×10^{-3}

963

964 **Table 3** Mean velocity, volume transport, near-bottom temperature, and near-bottom
 965 salinity from the models and from observations, for the time period when observations
 966 are available, as shown in Figs. 3,4. However, the values from ECCO2 are for 1992-
 967 2004 only and the values from ORCA are for 1990-2001 only. Error estimates are shown
 968 in parenthesis. All model errors are calculated as the standard error of the mean (sample
 969 standard deviation divided by the square root of the sample size).
 970
 971

Model/Data	Mean velocity ~10 m above bottom at the A2 location (cm/s)	Mean velocity ~10 m above bottom at the A3 location (cm/s)	Mean volume transport (Sv)	Mean temper- ature ~10 m above bottom at the A2 location (°C)	Mean temper- ature ~10 m above bottom at the A3 location (°C)	Mean salinity ~10 m above bottom at the A2 location (psu)	Mean salinity ~10 m above bottom at the A3 location (psu)
BESTMAS	33.1 (1.3)	21.8 (0.8)	0.69 (0.03)	0.79 (0.25)	0.65 (0.24)	33.16 (0.06)	33.20 (0.06)
Data	26.2 (2.8)	20.9 (2.3)	0.80 (0.20) ⁺	0.27 (0.3)	-0.11 (0.2)	32.26 (0.08)	32.49 (0.06)
ECCO2	39.4 (1.2)	26.9 (0.7)	1.06 (0.03)	1.10 (0.27)	0.62 (0.23)	31.72 (0.06)	32.29 (0.04)
NAME	33.0 (1.0)	26.2 (0.7)	0.67 (0.03)	-0.96 (0.09)	-1.26 (0.05)	32.45 (0.04)	32.61 (0.04)
ORCA	40.4 (1.9)	30.6 (1.3)	1.29 (0.06)	0.96 (0.25)	0.79 (0.24)	32.30 (0.05)	32.47 (0.03)
PIOMAS	28.6 (1.0)	29.9 (0.9)	0.81 (0.03)	0.34 (0.21)	0.60 (0.23)	33.09 (0.05)	32.80 (0.05)

+the uncertainty for the data estimate is ~25% (Woodgate et al. 2005a, b)

972
 973
 974
 975
 976
 977
 978
 979
 980
 981
 982
 983

984 **Table 4** Long-term mean velocity, volume transport, near-bottom temperature, and near-
 985 bottom salinity from the models, for the time periods shown in Figs. 3,4. Error estimates
 986 are shown in parenthesis.
 987

Model/Data	Mean velocity ~10 m above bottom at the A2 location (cm/s)	Mean velocity ~10 m above bottom at the A3 location (cm/s)	Mean volume transport (Sv)	Mean temperature ~10 m above bottom at the A2 location (°C)	Mean temperature ~10 m above bottom at the A3 location (°C)	Mean salinity ~10 m above bottom at the A2 location (psu)	Mean salinity ~10 m above bottom at the A3 location (psu)
BESTMAS	34.0 (0.69)	22.8 (0.45)	0.72 (0.02)	0.76 (0.17)	0.71 (0.16)	33.18 (0.05)	33.17 (0.04)
ECCO2	39.9 (0.78)	27.4 (0.52)	1.07 (0.02)	1.08 (0.25)	0.63 (0.20)	31.72 (0.05)	32.25 (0.03)
NAME	34.1 (0.52)	27.0 (0.65)	0.65 (0.01)	-1.02 (0.06)	-1.27 (0.03)	32.46 (0.02)	32.58 (0.02)
ORCA	43.2 (0.88)	31.6 (0.65)	1.33 (0.03)	0.89 (0.17)	0.69 (0.15)	32.33 (0.02)	32.47 (0.02)
PIOMAS	29.5 (0.49)	29.2 (0.49)	0.79 (0.02)	0.26 (0.14)	0.53 (0.15)	33.13 (0.03)	32.78 (0.03)

988
 989
 990
 991
 992
 993
 994
 995

Table 5 Correlation coefficients between models and the observations of velocity, temperature, and salinity at A2 and A3 locations. All correlations are significant at the 95% level.

Model	Velocity		Temperature		Salinity	
	A2	A3	A2	A3	A2	A3
BESTMAS	0.78	0.71	0.78	0.70	0.67	0.53
ECCO2	0.67	0.72	0.77	0.76	0.60	0.48
NAME	0.69	0.75	0.73	0.86	0.70	0.57
ORCA	0.68	0.70	0.79	0.76	0.60	0.39
PIOMAS	0.70	0.82	0.88	0.79	0.66	0.59

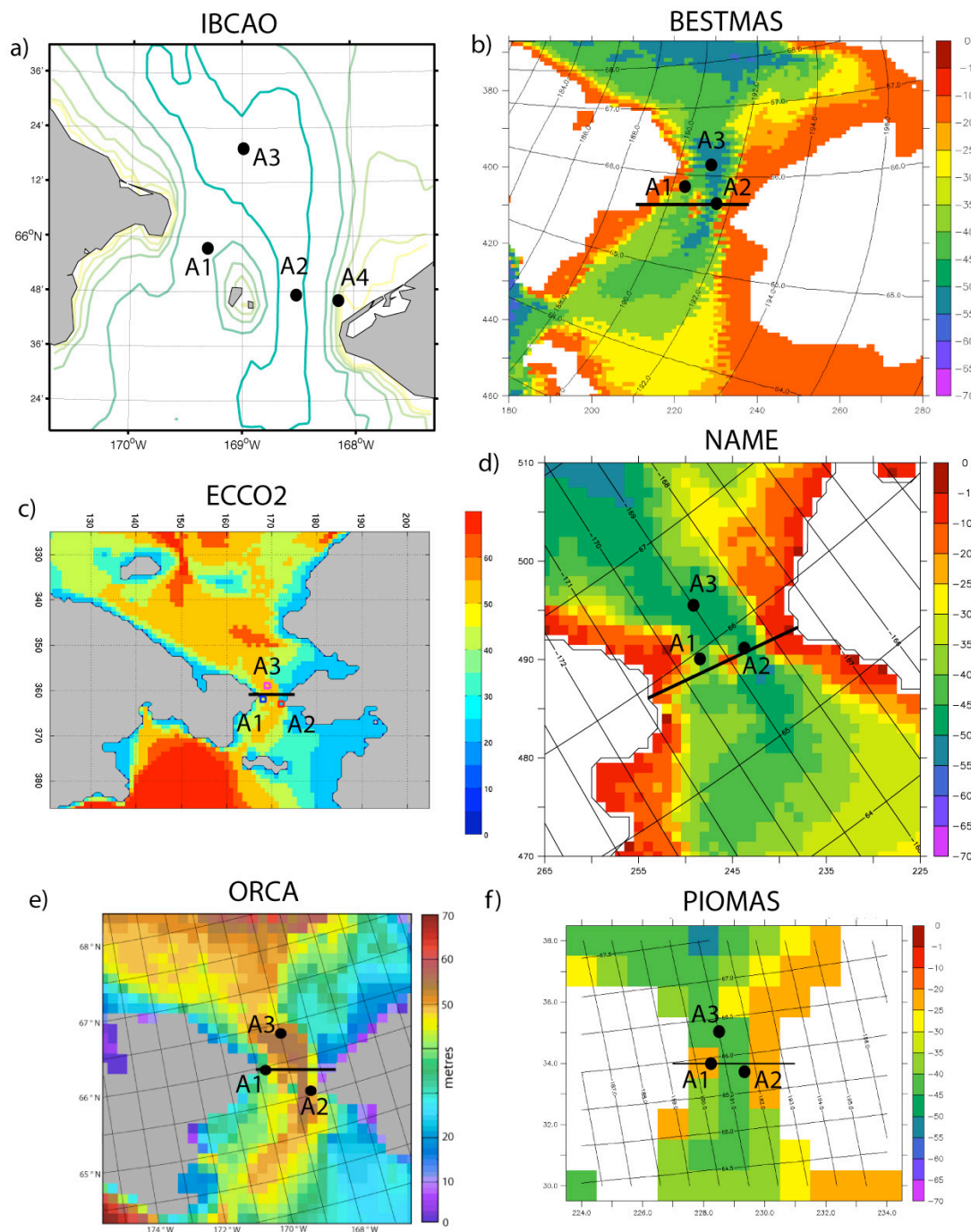
996
 997
 998
 999

1000
1001
1002

Table 6 Depth information (m) for the models and the observations at the A2 and A3 mooring locations.

Location	Model/data	Water column depth (m)	Mid-depth of model grid cell or depth of observation ~10 m above bottom (m)
A2	Data	53	44
	BESTMAS	51	39.5
	ECCO2	50	35
	NAME	53	37.7
	ORCA	57.9	35.5
	PIOMAS	43	33
A3	Data	56	47
	BESTMAS	51	39.5
	ECCO2	50	35
	NAME	53	37.7
	ORCA	57.9	35.5
	PIOMAS	43	33

1003
1004
1005
1006
1007
1008
1009
1010
1011
1012
1013
1014
1015
1016
1017
1018
1019
1020
1021
1022
1023
1024
1025
1026
1027



1029

1030

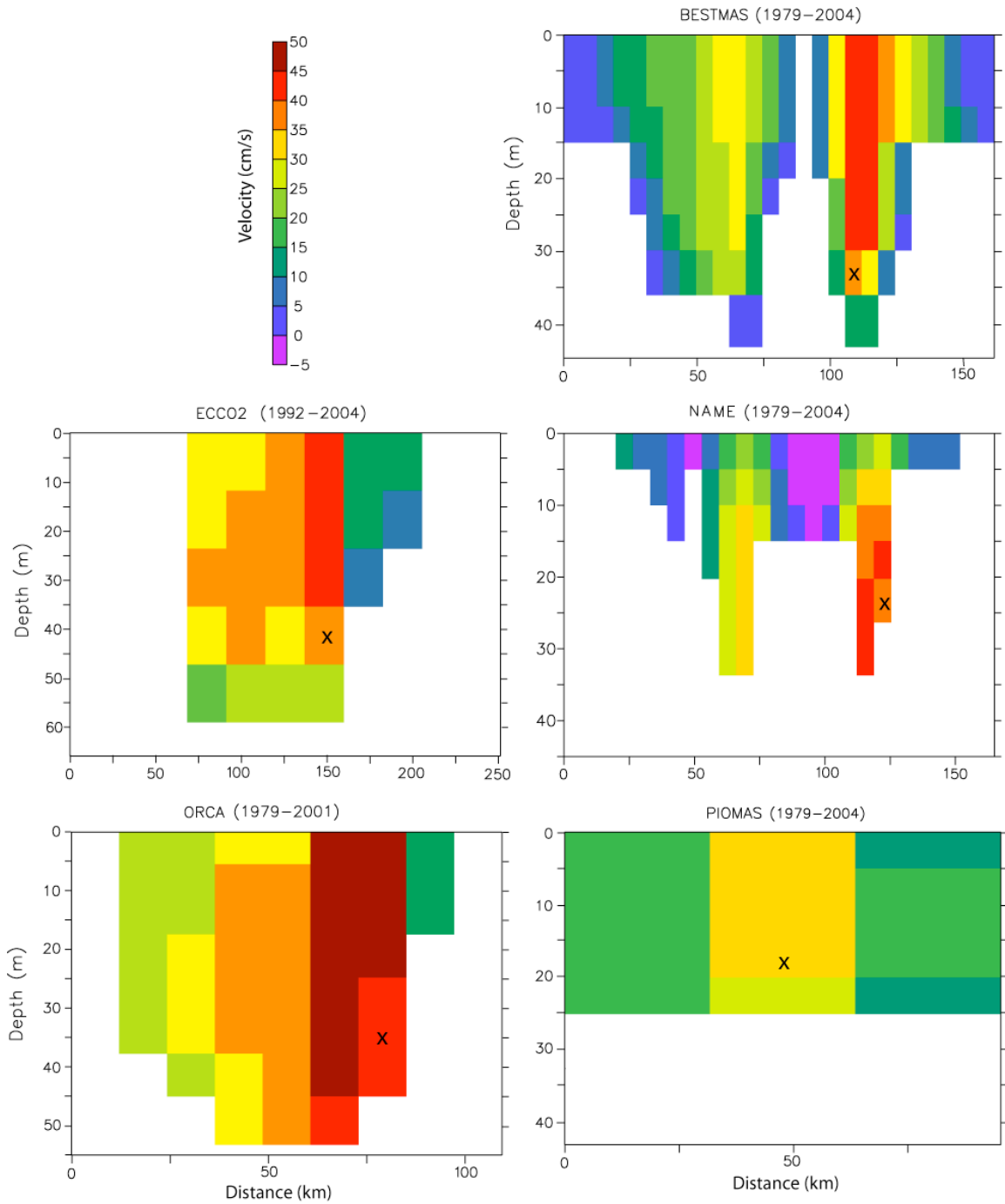
1031 **Fig 1** Bathymetry (m) in the vicinity of the Bering Strait (a). Depth contours are every

1032 10 m from the International Bathymetric Chart of the Arctic Ocean (Jakobsson et al.

1033 2000). Model bathymetry (m) from (b) BESTMAS, (c) ECCO2, (d) NAME, (e) ORCA,

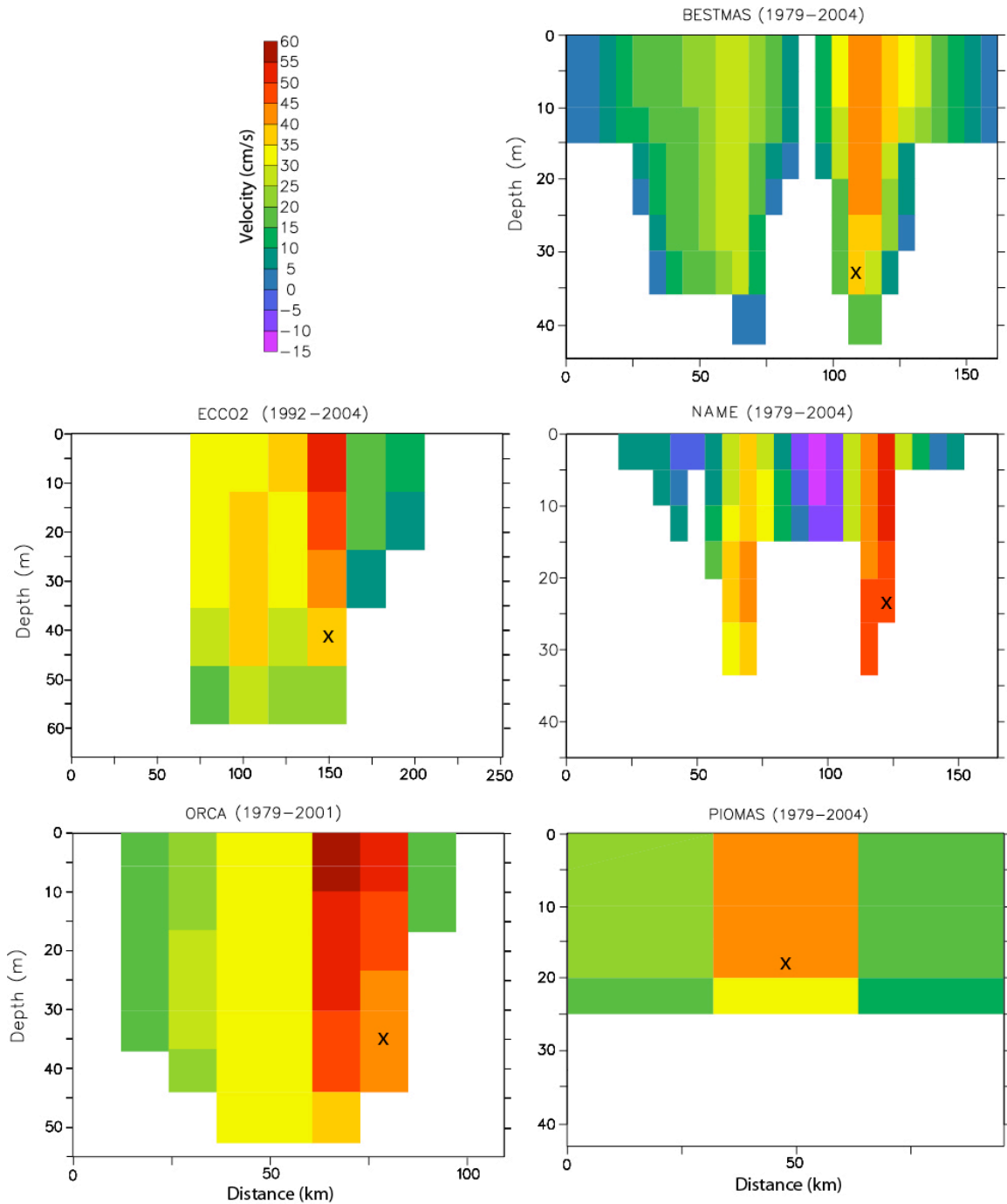
1034 and (f) PIOMAS. The approximate locations of the moored observations are indicated

1035 with black circles. The cross-sections across Bering Strait are shown as black lines in



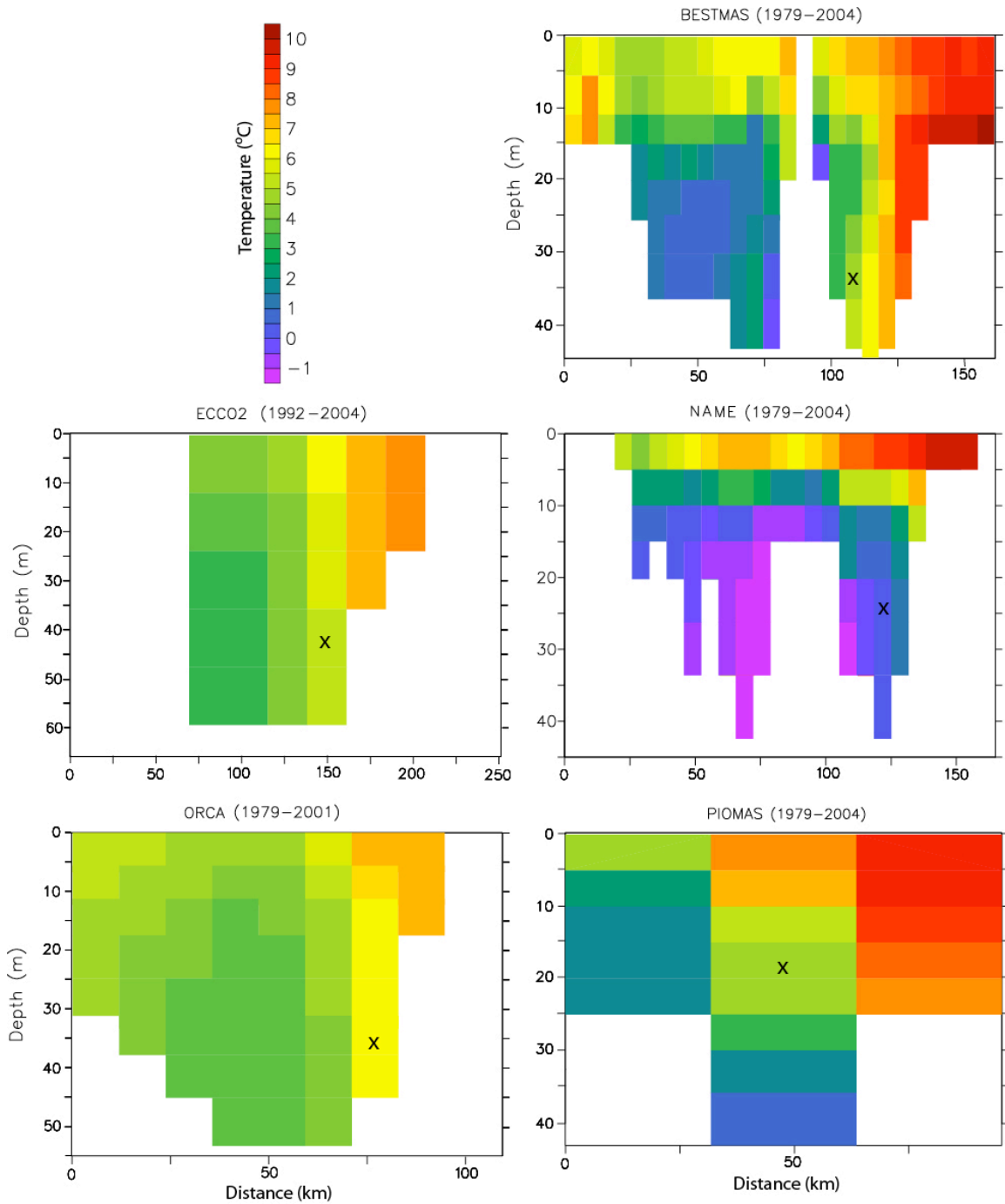
1036
 1037
 1038
 1039
 1040
 1041
 1042

Fig 2 Vertical section of the long-term mean northward velocity (cm/s) across Bering Strait from all models. Positive velocity is northward. A black X marks the approximate location of the A2 mooring within each model domain.



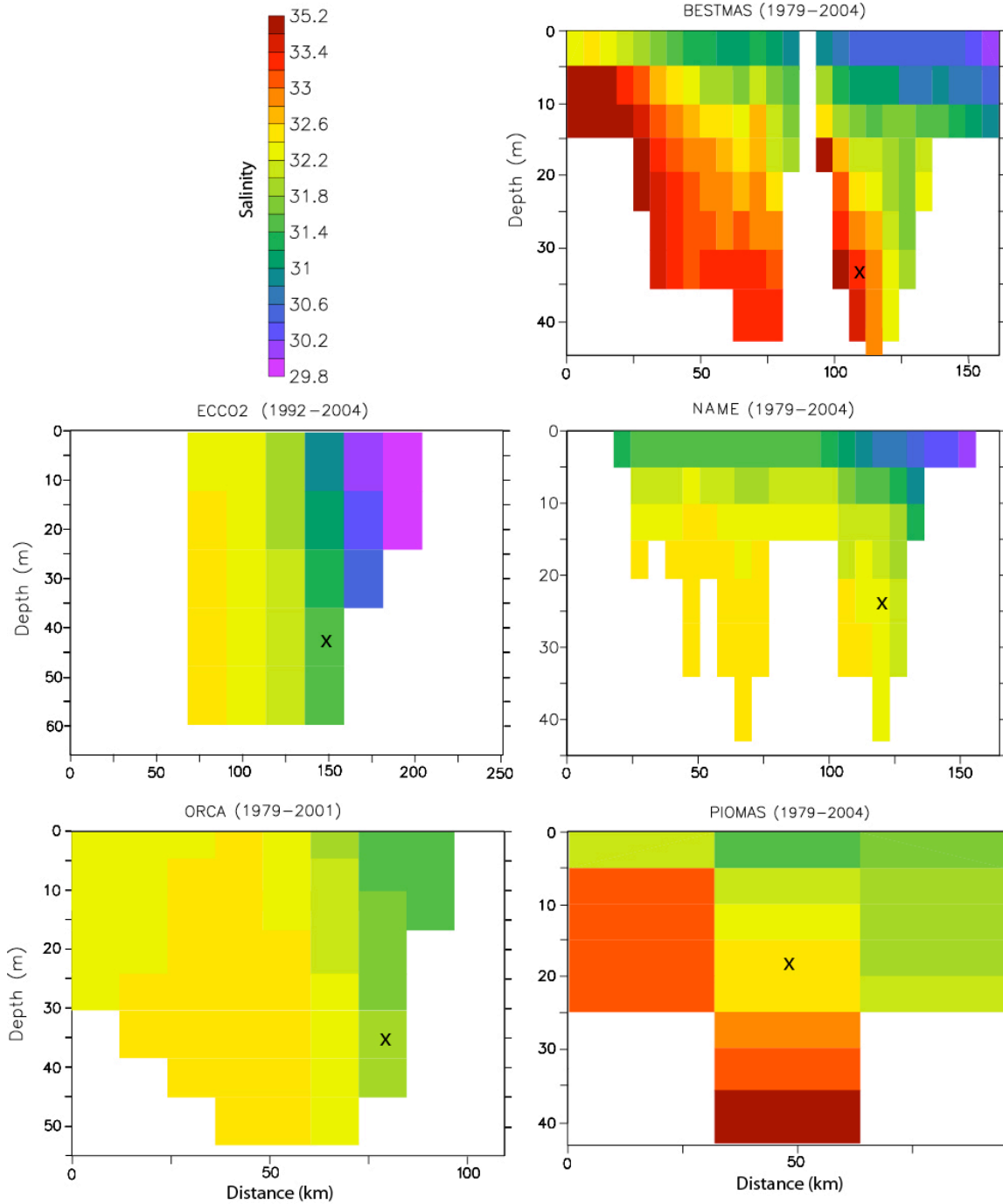
1043
 1044
 1045
 1046
 1047

Fig 3 Vertical section of the long-term summer (Jul.-Sep.) mean northward velocity (cm/s) across Bering Strait from all models. Positive velocity is northward. A black X marks the approximate location of the A2 mooring within each model domain.



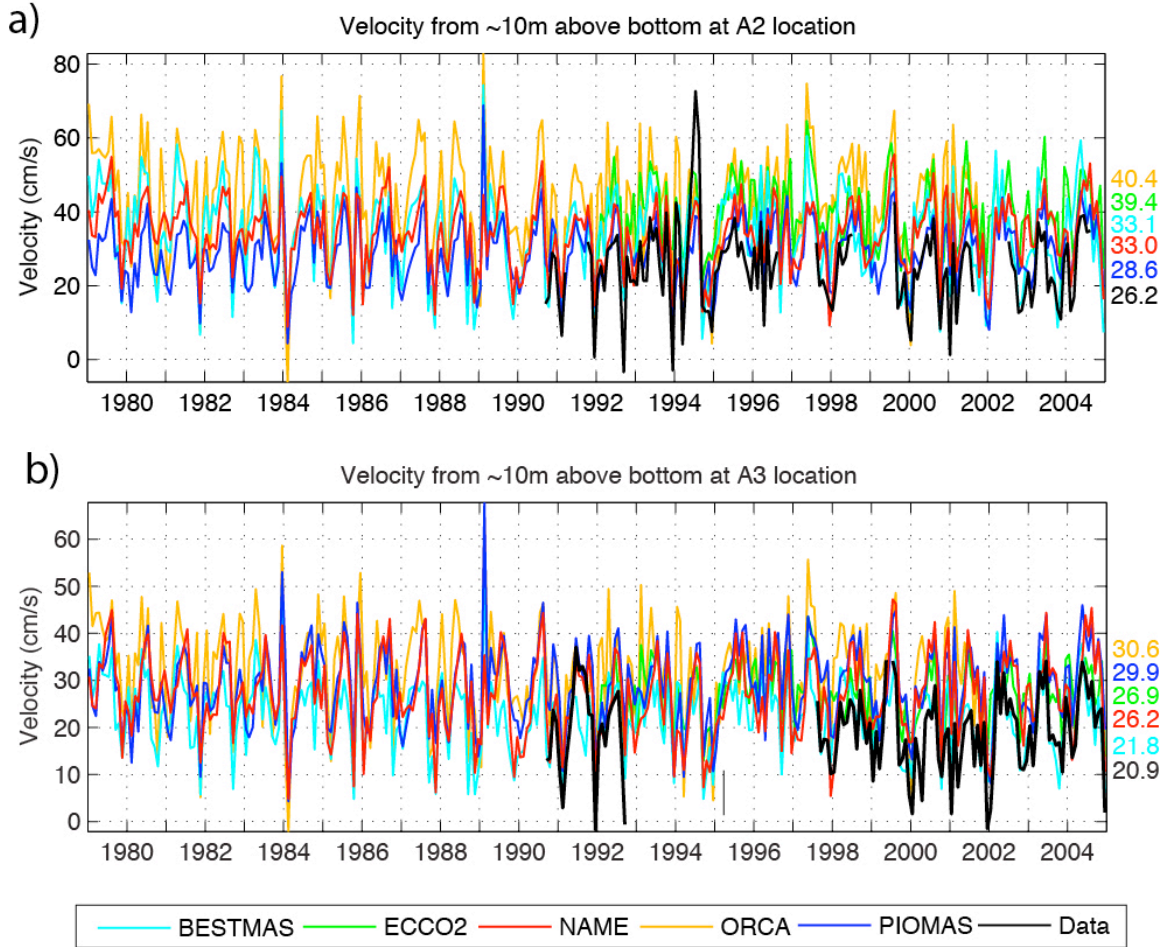
1048
 1049
 1050
 1051
 1052
 1053

Fig 4 Vertical section of the long-term summer (Jul.-Sep.) mean temperature ($^{\circ}\text{C}$) across Bering Strait from all models. A black X marks the approximate location of the A2 mooring within each model domain.



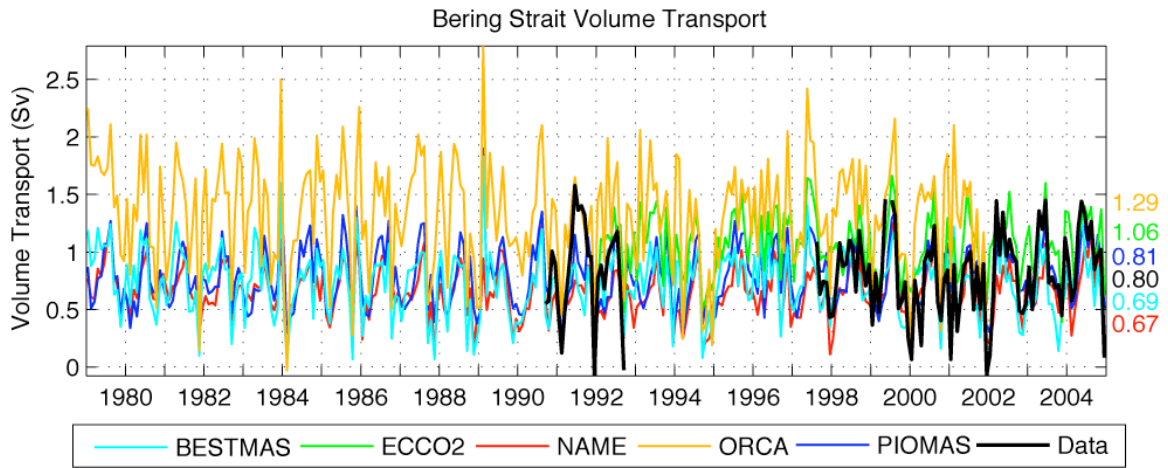
1054
 1055
 1056
 1057
 1058
 1059

Fig 5 Vertical section of the long-term summer (Jul.-Sep.) mean salinity (psu) across Bering Strait from all models. A black X marks the approximate location of the A2 mooring within each model domain.



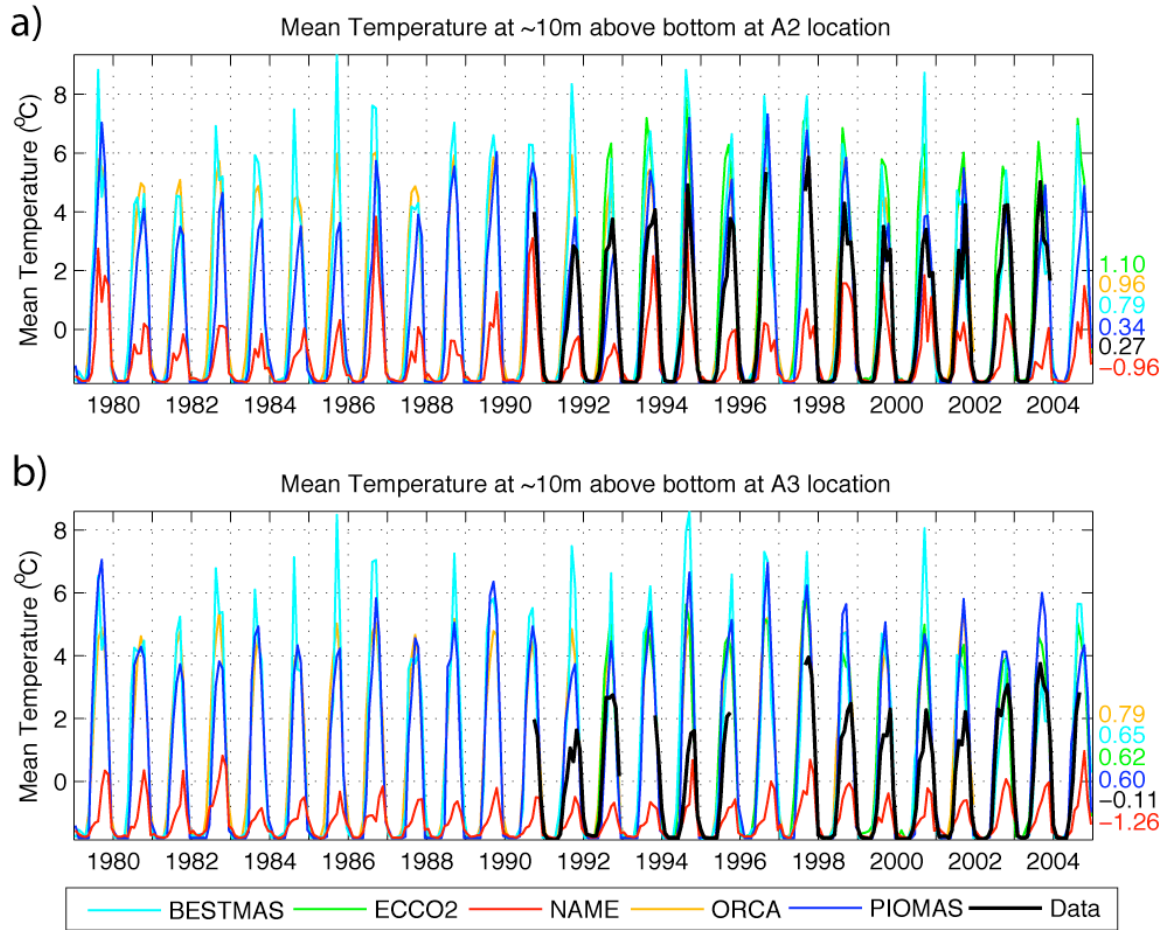
1060
1061
1062
1063
1064
1065
1066
1067
1068
1069

Fig 6 Monthly mean velocity at ~10 above the bottom from the A2 mooring location (upper) and A3 mooring location (lower). Model results are shown in color and the observations are shown in black. Mean values for the time period when data are available are shown on the far right.



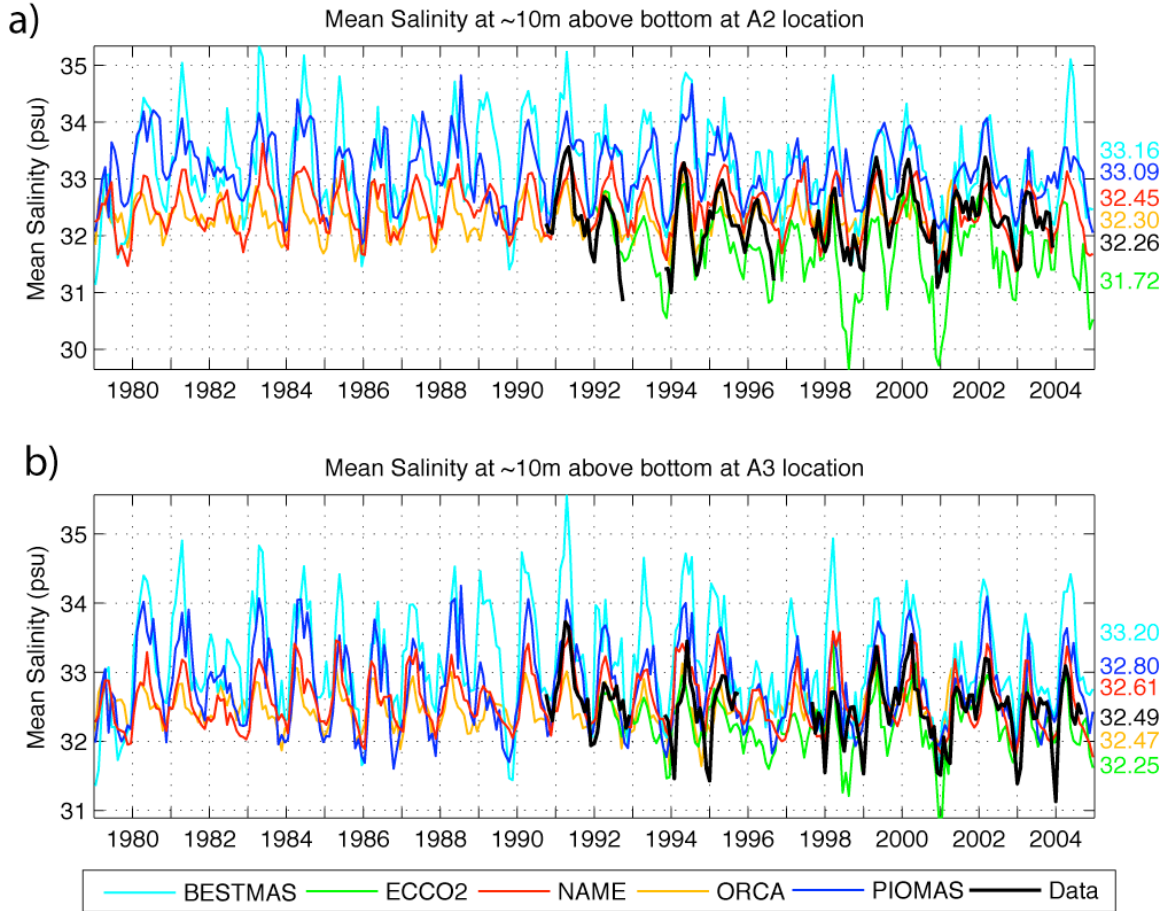
1070
1071
1072
1073
1074
1075
1076
1077
1078
1079
1080
1081
1082
1083

Fig 7 Monthly mean volume transport from the models and observations. The observations are based on the near-bottom velocity at the A3 mooring location multiplied by a cross-sectional area of 4.25 km^2 , as per Woodgate et al. (2010). Mean values for the time period when data are available are shown on the far right.



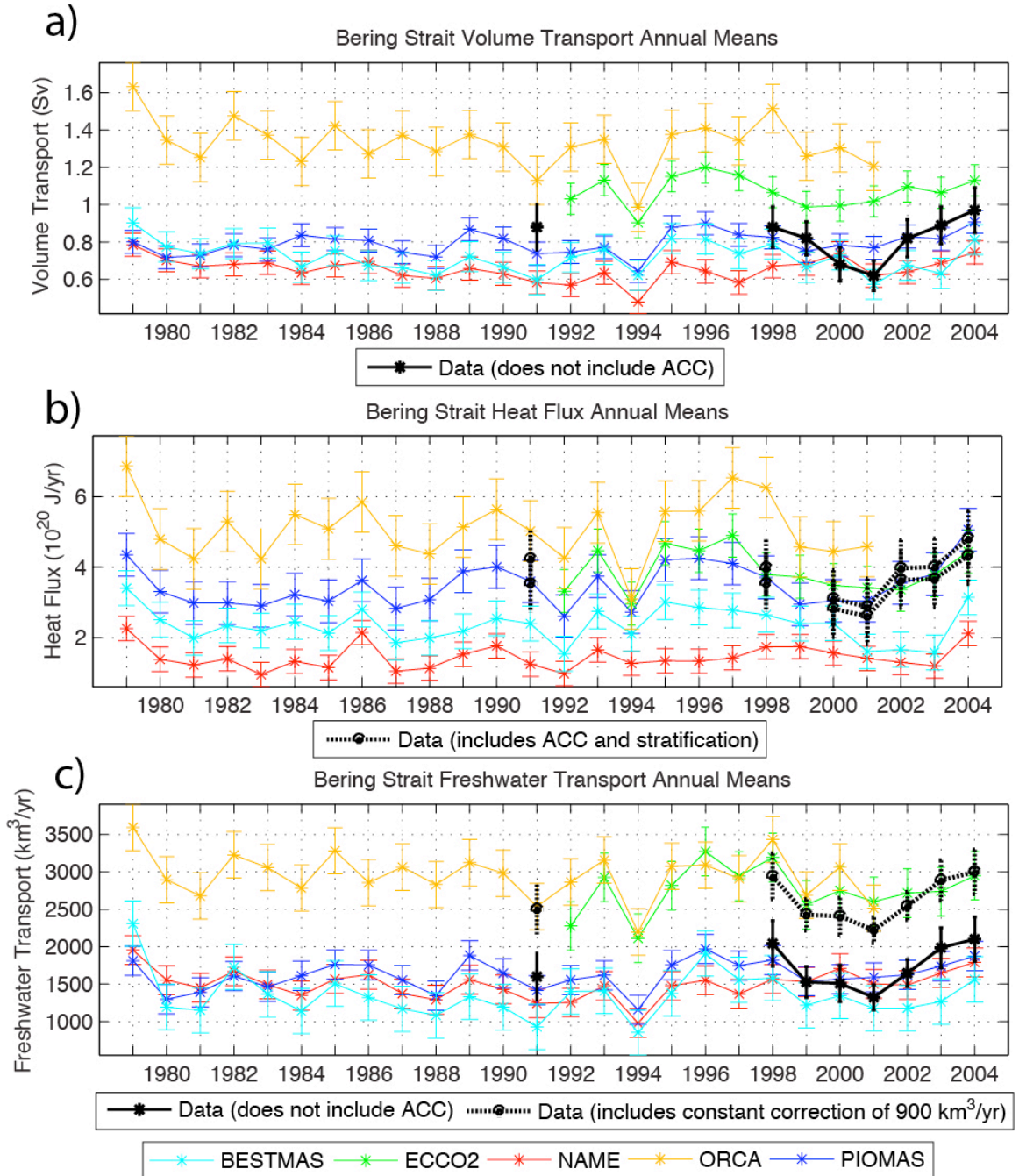
1084
1085
1086
1087
1088
1089

Fig 8 Monthly mean near-bottom temperature (°C) at the (a) A2 and (b) A3 mooring locations. Model results are shown in various colors and observations are shown in black. Mean values for the time period when data are available are shown on the far right.



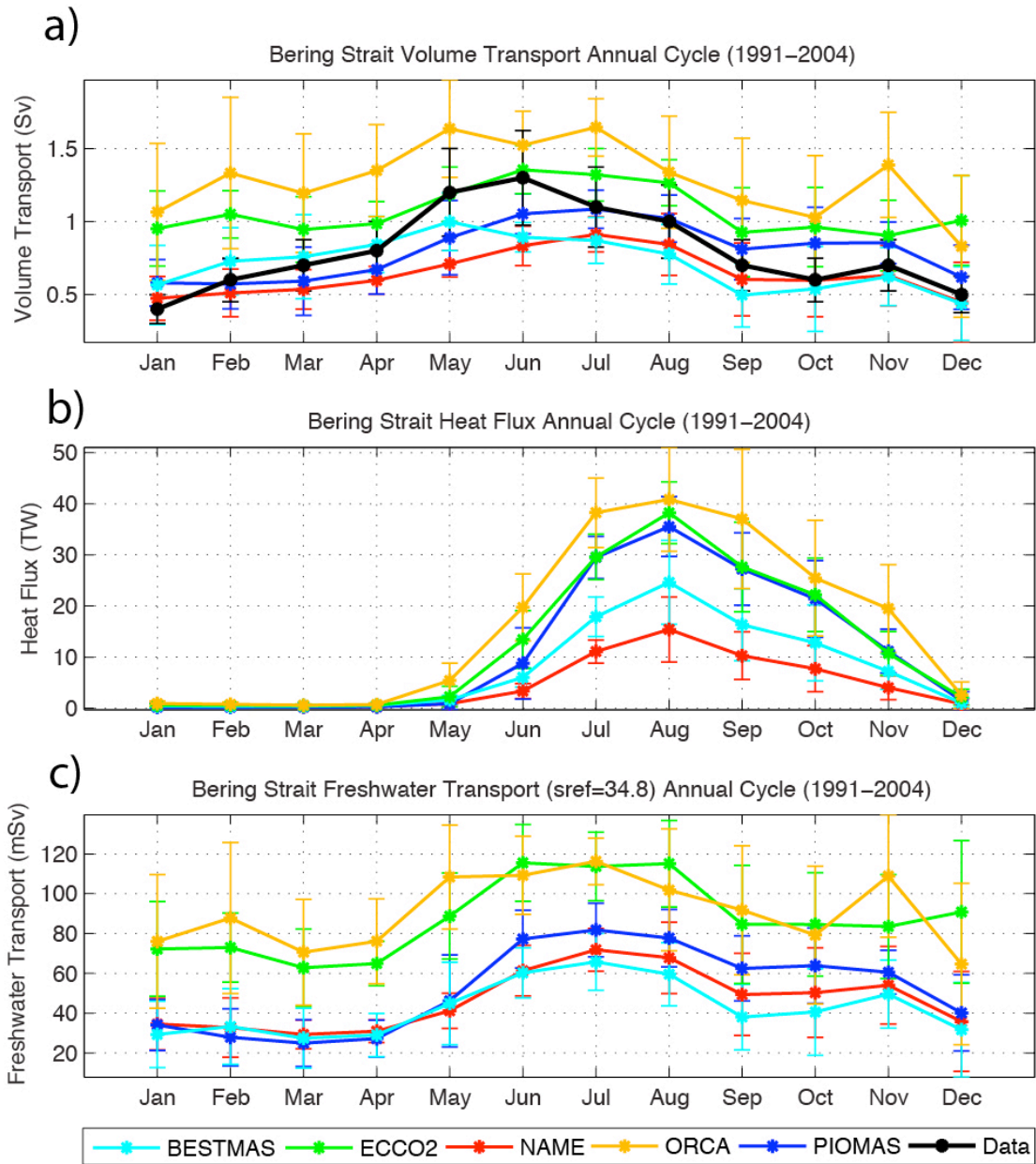
1090
1091
1092
1093
1094
1095

Fig 9 Monthly mean near-bottom salinity at the (a) A2 and (b) A3 mooring locations. Model results are shown in various colors and observations are shown in black. Mean values for the time period when data are available are shown on the far right.



1096
 1097
 1098
 1099
 1100
 1101
 1102
 1103
 1104
 1105
 1106

Fig 10 Annual mean (a) volume transport, (b) heat, and (c) freshwater fluxes. Heat flux is referenced to $-1.9\text{ }^{\circ}\text{C}$ for the models, in order to compare with cited observations in the text. Freshwater is referenced to 34.8 psu. Observed volume transport values (a) do not include the ACC and stratification, which likely add $\sim 0.1\text{ Sv}$ (see Woodgate et al. 2006). The observed heat flux values (b) include an estimate for the ACC using SST for a 10m surface layer (lower bound) and a 20m surface layer (upper bound). Observed heat flux values are described further in Woodgate et al. (2010). The dashed black line (c) represents the observed freshwater flux with an estimated ACC and stratification correction of an additional $900\text{ km}^3/\text{yr}$ (Woodgate et al. 2006).



1107
 1108
 1109
 1110
 1111
 1112
 1113
 1114
 1115

Fig 11 Seasonal cycles of (a) volume transport, (b) heat flux, and (c) freshwater transport. The seasonal cycles are averaged over 1991-2004, except for ORCA (1991-2001) and ECCO2 (1992-2004). Heat flux is referenced to $-1.9\text{ }^{\circ}\text{C}$ for the models, in order to compare with cited observations in the text. The freshwater transport is referenced to 34.8 psu.